Behavioral immune landscapes of inflammation

Georgiana Crainiciuc[1]*, Miguel Palomino-Segura[1]*, Miguel Molina-Moreno[2]±, Jon Sicilia[1,3]±, David G. Aragones[4], Jackson LiangYao Li[1,5], Rodrigo Madurga[6], José M. Adrover[1], Alejandra Aroca-Crevillén[1], Sandra Martin-Salamanca[1], Alfonso Serrano del Valle[1], Sandra D. Castillo[7,8], Heidi C.E. Welch[9], Oliver Soehnlein[10], Mariona Graupera[7,8], Fátima Sánchez-Cabo[3], Alexander Zarbock[11], Thomas E. Smithgall[12], Mauro di Pilato[13], Thorsten R. Mempel[13], Pierre-Louis Tharaux[14], Santiago F. González[15], Angel Ayuso-Sacido[6,16], Lai Guan Ng[5], Gabriel F. Calvo[4], Iván González-Díaz[2], Fernando Díaz-de-María[2] and Andrés Hidalgo[1,17]†

[1] Area of Cell and Developmental Biology, Centro Nacional de Investigaciones Cardiovasculares Carlos III, Madrid (Spain)
[2] Department of Signal Processing and Communication, Universidad Carlos III de Madrid, Madrid (Spain)
[3] Bioinformatics Unit, Centro Nacional de Investigaciones Cardiovasculares Carlos III, Madrid (Spain)
[4] Department of Mathematics & MOLAB-Mathematical Oncology Laboratory, Universidad de Castilla-La Mancha, Ciudad Real 13071, Spain
[5] Singapore Immunology Network (SIgN), A*STAR, Biopolis, Singapore
[6] Faculty of Experimental Sciences and Faculty of Medicine Universidad Francisco de Vitoria, 28223 Madrid, Spain.
[7] Endothelial Pathobiology and Microenviroment Group, Josep Carreras Leukaemia Research Institute (IJC), 08916 Badalona, Barcelona, Catalonia, Spain.
[8] Centro de Investigación Biomédica en Red de Cáncer (CIBERONC), Instituto de Salud Carlos III, Av. de Monforte de Lemos, 5, 28029, Madrid, Spain
[9] Signalling Programme, Babraham Institute, Cambridge, UK
[10] Institute for Experimental Pathology, Center for Molecular Biology of Inflammation, Westfälische Wilhelms-Universität, Münster, Germany.
[11] Department of Anesthesiology, Intensive Care and Pain Medicine, University Hospital Münster
[12] Department of Microbiology and Molecular Genetics, University of Pittsburgh, School of Medicine, Pittsburgh, Pennsylvania, USA.
[13] Center for Immunology and Inflammatory Diseases, Massachusetts General Hospital, Boston, Massachusetts, USA
[14] Université de Paris, Paris Cardiovascular Center, Inserm, Paris, France
[15] Institute for Research in Biomedicine, Università della Svizzera Italiana, Bellinzona, Switzerland
[16] Brain Tumor Laboratory, Fundación Vithas, Grupo Hospitales Vithas, 28043 Madrid, Spain
[17] Vascular Biology and Therapeutics Program and Department of Immunobiology, Yale University School of Medicine, New Haven, United States of America.

* and ±, these authors contributed equally as first and second authors, respectively
Corresponding author: Andres Hidalgo, ahidalgo@cnic.es

Abstract

Transcriptional or proteomic profiling of individual cells have revolutionized interpretation of biological phenomena by providing cellular landscapes of healthy and diseased tissues. These approaches, however, fail to describe dynamic scenarios in which cells can change their biochemical properties and downstream "behavioral" outputs every few seconds or minutes. Here, we used 4D live imaging to record tens to hundreds of morpho-kinetic parameters describing the dynamism of individual leukocytes at sites of active inflammation. By analyzing over 100,000 reconstructions of cell shapes and tracks over time, we obtained behavioral descriptors of individual cells and used these high-dimensional datasets to build behavioral landscapes. These landscapes recognized leukocyte identities in the inflamed skin and trachea, and inside blood vessels uncovered a continuum of neutrophil states, including a large, sessile state that was embraced by the underlying endothelium and associated with pathogenic inflammation. Behavioral in vivo screening of thousands of cells from 24 different mouse mutants identified the kinase Fgr as a driver of this pathogenic state, and genetic or pharmacological interference of Fgr protected from inflammatory injury. Thus, behavioral landscapes report unique biological properties of dynamic environments at high cellular, spatial and temporal resolution.

Fundamental biological phenomena, such as those associated with development or immunity, require the concerted migration, adhesion, signaling and molecular or functional reprogramming of cells. Single cell "omics" technologies that measure the transcriptome and proteome have enabled the reconstruction of persistent cellular states and identities with extraordinary precision and resolution, in turn yielding valuable information on the biological processes under study [1]. These technologies, however, cannot capture rapid transitions between cellular states in highly dynamic scenarios, such as those seen during acute inflammatory responses. Indeed, inflammation is characterized by the presence of leukocytes undergoing constant changes in motility and morphology as they adapt to local cues (e.g., cytokines or chemokines) and anatomical barriers (such as matrix fibers, vessels or other neighboring cells), and rely on pre-existing molecular programs (e.g., different cell lineages expressing or not certain receptors). For this reason, accurate mapping of such processes demands spatial tracing of the same cells over time, which is not possible with traditional single cell omics technologies.

Dynamic features of physiological processes have been traditionally captured by direct live imaging of the affected tissues [2]. Although microscopic imaging is endowed with single cell resolution, very few parameters are typically extracted from these experiments and cells are analyzed as homogeneous populations, resulting in poor yields of biological information. Critically, however, how a cell moves and changes shape (i.e., behaves) is the result of genetic and signaling networks that vary across tissues and cell types [3], and should therefore contain information about core features of the cell. For example, cell navigation in complex three-dimensional microenvironments relies on nuclear positioning and microtubular probing, integrin activation and the actin cytoskeleton, as well as a full array of kinases, regulatory factors and upstream receptors that sense and coordinate the response of cells in their native environment [4].

We therefore posited that the behavioral traits of individual cells within living tissues contain precious biological insights about the identity (transcriptional signature) and state (active signaling pathways) of the cells. Here, we show that functional immune identities and states can be at least in part inferred from the behavioral pattern of cells in living tissues, in turn allowing the generation of cellular landscapes of dynamic biological processes at the single cell level with high temporal and spatial resolution.

Behavioral landscapes capture leukocyte identities in vivo

Because the dynamic behavior of a cell is the result of its genetic, protein and general metabolite content, we postulated a model whereby multiple behavioral traits can be integrated to describe and predict meaningful biological properties of cells in living tissues (Figure 1A), such as cell identities or functional states. To test this idea, we made use of a series of existing [5,6] and new imaging experiments in defined tissues and inflammatory contexts, in which myeloid cells (neutrophils, dendritic cells or DCs for all experiments, and macrophages for ischemic inflammation) expressed cytoplasmic fluorescent proteins (GFP, CFP or YFP; see Methods) that allowed precise measurement of their morphology and movement in a three-dimensional space over time through multiphoton in vivo microscopy.

We first imaged cells in the trachea of mice infected with influenza virus (PR8 strain) and used the Imaris software to extract 118 parameters describing features of motion and shape of thousands of individual cells, at multiple temporal instants (Figure 1B and Movie S1). We generated a correlation network to visualize the distribution of all parameters and facilitate supervised selection of those that best described cellular behaviors (Extended Data Fig.1A-D). The selected 31 parameters (19 kinetic and 12 morphometric; see a full list in Data S1, and heatmap in Extended Data Fig.2A-B) were used to generate a tSNE map that revealed two dominant groups of cells based on their behavior and, importantly, separability of the cells into these clusters was proportional to the number of parameters used in our analysis (Figure 1C). Because our datasets contained independent information on the leukocyte identities (YFP for DCs, CFP for neutrophils) that was not used for our initial classification, we could now employ this feature to estimate the accuracy of the behavioral modeling in matching cell identities. We found that both classifications were essentially overlapping (Figure 1D) and used this information to build a qualitative stochastic approach (see details in Methods) modeling the relationship between the percentage of known behavioral parameters and knowledge of a biological system (Figure 1E), in this case the identity of leukocytes in the infected trachea. Likelihood ratio indexes (LRIs) obtained from a logistic model revealed a learning curve (exponential-like banded) between the knowledge that could be inferred from our biological system and the percentage of behavioral variables used. For example, from 10 randomly-selected parameters only about 60% of the system (cell identities) could be inferred, whereas full knowledge (perfect score for every cell) was possible with all 118 parameters (Extended Data Fig.2C). Of note, although data analysis using all the parameters through a standard single cell analytical pipeline yielded good cell classification, we found that parameter down-sampling still improved cell classification by avoiding inclusion of parameters that were redundant or arbitrary, and ensuring that both morphometric and kinetic features were included (Extended Data Fig.1E-G).

Our multidimensional analyses and logistic mathematical models further allowed us to examine the specific parameters that best discriminated leukocyte identities and clusters based on behavior (Figure 1F-G). Interestingly, dynamic changes in speed (Track Speed Variation, shown in Figure 1F) was a better predictor of cell identity than parameters that directly measured cell size and speed. These findings underlined the power of unbiased behavioral measures of native cells in vivo, identified behavioral change as a major store of biological information, and allowed us to refine our correlation networks to include the importance of each parameter based on its LRI (shown in networks and as a heatmap in Extended Data Fig.1B-D) in scoring biological identities. Using expression plots and Pearson correlation matrices we were also able to infer specific biological features of interest in the infected trachea. For instance, we noticed that straight and fast movement were featured by different groups of neutrophils, that neutrophils moved slower in the vicinity of DCs, or that DCs displayed highly homogeneous behaviors (Extended Data Fig.2D-E).

We next tested these behavior-based single cell analyses in models of ischemia-reperfusion (I/R) and laser burn injury in the skin [5–7] using the same set of parameters (Movies S2 and S3). In the I/R injury model, integrated behavioral profiling identified 3 major clusters largely matching the known cell types (neutrophils, DCs and macrophages; Figure 1H and Extended Data Fig.3A-B). Further sub-clustering allowed identification of two types of behaviorally distinct neutrophils, two types of DCs (CD11c+ cells), and three types of macrophages (Extended Data Fig.3B-C). As an example, this behavior-based classification identified neutrophil types with marked differences in navigation velocity and size, and a type of CD11c+ DC with macrophage-like behavior (Extended Data Fig.3B). Behavioral analyses may therefore complement reporter models for a more accurate in vivo classification of immune cells. In the laser injury model, we could again discriminate neutrophils from DCs with high accuracy (Figure 1I) and found distinct behavioral patterns in neutrophils as they swarmed and got closer to the injury site (Extended Data Fig.4A-C). Because the generated dataset also contained spatial information for each cell, it allowed us to build "behavioral maps" in which we projected selected parameters or clusters of interest onto individual cells in their actual location, thus allowing the association of individual behavioral traits (Extended Data Fig.4D) or complex behavioral patterns (Extended Data Fig.4E) with anatomical hallmarks of the tissue. In the I/R dataset, for example, these maps allowed us to visualize the distribution of the behaviorally-distinct macrophages, DCs and neutrophils into ischemic and non-ischemic regions of the skin (Extended Data Fig.3D, bottom panels). Finally, we found that the morpho-kinetic analyses also allowed robust classification of morphologically-similar subsets of T cells in a tumor (Extended Data Fig.4F-G), and unveiled behavioral changes as the same cell type moved through different anatomical microenvironments (Extended Data Fig.4H-J).

Together, this set of experiments validated the efficacy of behavioral tracing in deciphering immune properties in vivo, and suggested that they could complement single cell technologies endowed with greater molecular depth, but lacking spatial and dynamic information.

Behavioral landscape of intravascular neutrophils

While leukocyte identities can be efficiently defined using stable genetic lineage drivers, such as CD11c or LyzM as in the above experiments, they fail to capture activation states of a given cell lineage. In turn, use of genetic or chemical probes targeting specific signaling pathways in vivo exist but are scarce, not fully specific and prone to artifacts, and often provide unidimensional information [8,9]. We considered cell states critical to define highly dynamic settings in which changes in cell activation occur rapidly, particularly for cell subsets such as neutrophils, in which subtle changes in the proteomic or transcriptomic content can have a profound influence in the outcome of inflammation [10,11].

We therefore challenged our model to generate behavior-driven landscapes for neutrophils in a model of acute vascular inflammation induced by TNFα. In this model, neutrophils are the most abundant leukocytes [12] and can be imaged with high spatial and temporal resolution by spinning-disk confocal imaging in the cremaster muscles of LyzM[GFP] mice (Figure 2A and Movie S4) [13]. To improve accuracy and remove bias in the measurement of morphological and kinetic traits as well as distances to the vessel wall (labeled in vivo with anti-CD31 antibody; [13]) we implemented a custom-built analytical tool based on machine learning (ACME, see Methods) that yielded 73 parameters (48 kinetic and 25 morphometric; Data S1) which we used to describe the behavior of hundreds of cells over time (Figure 2B-C).

Visualization of this dimension-rich dataset in UMAP plots revealed three major behavioral clusters (Figure 2D-E). To enhance the biological relevance of our approach, we repeated our analyses in mice that were protected from acute inflammatory injury by depleting platelets before TNFα treatment, as stochastic interactions with platelets are known to trigger activating, pro-inflammatory activity in intravascular neutrophils [14]. By integrating this dataset with that of control mice, we confirmed the presence of three main behavioral clusters (B1-B3; Figure 2E). Notably, we noticed that B1 was strongly increased in platelet-depleted mice, B3 dominated in inflammation-prone control mice, and B2 was common to both groups (Figure 2D-F). Neutrophils from control mice appeared in all three behavioral groups (density plots in Figure 2D), suggesting that all types of behavior coexist, and that preventing pathogenic inflammation preferentially targeted B3 behaviors.

Careful examination of the behavioral parameters defining each cluster revealed that cells in B1 were more spherical, had their center mass more distant to the vessel wall and a higher height-to-length ratio (referring to cell extension towards the lumen relative to that in contact with the vessel wall; Figure 2B and 2G). Cells in B3, in contrast, were the largest in size (length, area and volume), had an oblate morphology and their center mass were very close to the vessel wall. Cells in both B1 and B3 featured low speeds and were often sessile. Finally, cells in the common B2 group were characterized by rapid movement and, particularly, by highly dynamic changes in movement and shape as indicated by high values in standard deviations for most parameters (Figure 2B and 2G). These behavioral analyses defined neutrophils associated with the platelet-depleted group (B1) as small, egg-shaped cells standing motionless on the vascular wall, whereas those in the shared behavioral group (B2) were ameboid-shaped, fast-moving and featured frequent changes in shape and pace

(Figure 2H and Movie S5). Close analysis of cells from B2 in fact revealed that these cells advanced with inchworm-type steps, following conspicuous stretch-shrink cycles (Extended Data Fig.5A and Movie S5), a type of movement that explained their highly variable morphological and kinetic traits. Finally, cells associated with active inflammation in control mice (B3) were large and sessile, in intimate contact with the vasculature. This close apposition to the vessel wall was further evidenced by the presence of "footprints" on the endothelial substrate (Figure 2I) as well endothelial extensions covering part of B3 neutrophils (Extended Data Fig.5B), none of which were observed in cells from B1 or B2 (Figure 2I and Extended Data Fig.5B). We could confirm these behavioral patterns using a different neutrophil-specific reporter mouse line (Ly6G^{Cre}; Rosa26^{tdTom}; Extended Data Fig.5C-D) [15]. Importantly, the behavioral patterns identified in our analyses matched activation states of intravascular neutrophils defined by surface expression of CD11b and phagocytosis of albumin-coated beads [16], which predominated in B1 and progressively declined in B2 and B3, and were at baseline in rolling neutrophils (Extended Data Fig.5E-F). Further, we found that although B3 neutrophils typically localized near endothelial junctions, only a very small fraction crossed the vascular wall into the inflamed tissue, whereas B2 neutrophils transmigrated more efficiently, and those in B1 did not extravasate (Extended Data Fig.5G-I).

While all cells in B2 featured highly variable behaviors in movement and shape, we noticed heterogeneity within this behavioral group and therefore performed hierarchical classification to identify additional states within this group. This approach revealed three distinct sub-behavioral profiles within B2 (B2.1, B2.2 and B2.3) (Extended Data Fig.6A-B). All sub-clusters maintained the dynamism typical of the B2 cluster, but noticeably featured morphological properties and distances to the vascular wall reminiscent of either the B1 or the B3 groups (Extended Data Fig.6C), suggesting highly dynamic transitions between the different behavioral groups. We took advantage of stored information in our dataset of tracks corresponding to the same cell over time (i.e., the behavioral history of each cell) and asked whether the same neutrophil could transition between the different behavioral clusters or instead cells were behaviorally stable (i.e. remained always in the same behavioral group). We found that transitions between behaviors were surprisingly frequent, with up to one fourth of cells (17-24%) changing behavior during our observation period (~6-8 min), particularly when cells were in B2, or within different B2 sub-behaviors (23%; Extended Data Fig.6D). In contrast, direct transitions between the extreme behaviors (B1 and B3) were rare (4%), suggesting that B1 and B3 are extremes of a behavioral continuum, and that B2-type behaviors represent transitional states of intravascular neutrophil (Extended Data Fig.6E).

Genetic regulators of intravascular behaviors

The identification of neutrophil states associated with vascular inflammation (B3) offered the possibility to screen for drivers of inflammogenic behaviors by scoring key morphological traits defining each group in static, three-dimensional imaging inside TNFα-treated vessels. Among the features that best discriminated cells across the different behavioral groups we chose the cell's main axis relative to the endothelial

surface (height-to-length or H/L ratio) as this strongly discriminated cells in B1 from those in B3, as well as the prolate shape, which was typical of the non-inflammatory groups (B1 and B2; see full list of differentially scored parameters in Extended Data Fig.7A). We also performed experiments to extract kinetic parameters of fast- vs. slow-moving cells (discriminating B2 from B1 and B3; Extended Data Fig.7A). Using these criteria, we first tested these specific parameters in conditions known to protect from inflammatory injury by preventing neutrophil activation inside vessels, including the platelet-depletion model and mice lacking the receptor PSGL-1 (*Selplg*−/−; [14]). We found that both conditions consistently increased H/L ratios, decreased prolate shapes, and restricted cell movement of intravascular neutrophils, all of which were consistent with neutrophils transitioning away from B3 and towards B1-type behaviors (Figure 2G).

We then used the traits associated with the pathogenic B3 behavior for a large in vivo screening effort comprising 24 mutant mouse lines defective in genes involved in different stages of neutrophil activation (Table S1 and [17]). These included mutants for 4 additional surface receptors, 3 adaptor and 3 Src-family kinases, as well as 12 downstream signaling kinases, small GTPases and exchange factors (Figure 3A). We used these mutants together with DsRed+ wild-type donors to generate mixed chimeric mice by bone marrow transplantation, as this allowed us to use DsRed+ neutrophils as internal reference in each mouse. Analysis of >3700 individual cells in the mutant and reference groups (total 27 groups) for kinetic and morphological features (Figure 3B, Extended Data Fig.7 and 8) yielded a neutrophil behavioral map associated with each mutant or treatment (Figure 3C). Hierarchical clustering of this matrix revealed a group of 5 genes whose loss led to anti-inflammatory profiles reminiscent of those seen in the platelet-depletion and PSGL-1-deficient groups (Figure 3C). Two of these genes encoded for activating receptors (Fpr1 and CXCR2), two were upstream signaling regulators (Fgr, and combined deficiency in the adaptors Fcgr and Tyrobp), and one encoded for the small GTPase Rap1a. The overrepresentation of membrane-proximal molecules among the positive hits (receptors and adaptors; asterisks in Figure 3A) suggested that intravascular behaviors are imprinted early in the signaling cascade, either at the receptor level or immediately downstream of the receptors, including those that bind chemokines and selectins [14,18]. Given the finding that intravascular neutrophils frequently transit between behavioral states (Extended Data Fig.6D-E), these results also suggested that dynamic on/off engagement of behaviors is dominated by a relatively small repertoire of molecules and signaling pathways, and therefore raised the possibility to target them to protect from vascular inflammation.

Behavioral reprogramming blunts inflammation

Among the genes identified in our behavioral screening we focused on *Fgr* because this Src-kinase has not been previously associated with impaired recruitment, recognition of danger, or with altered inflammatory states as is the case for the other genes [17,19]. Indeed, in our hands Fgr-deficient neutrophils were recruited to sites of inflammation and produced NETs as efficiently as wild-type cells (Extended Data Fig.9A-B). Focus on a single gene (rather than the dual adaptor mutant, for example) additionally provided a more amenable target for pharmacological intervention.

To confirm that Fgr-mediated signaling controlled the behavioral landscape of intravascular neutrophils, we generated Fgr^{-/-} mice bearing a cytoplasmic reporter protein to allow for prolonged 4D imaging, extraction of morpho-kinetic cell features, and generation of behavioral landscapes of intravascular neutrophils (Figure 4A-B). In line with our screening (Figure 3), we found marked behavioral shifts for Fgr-deficient neutrophils from B3 to B2 (rather than to B1; Figure 4A-B), which was consistent with the preferred transitions occurring between these two types of behaviors (Extended Data Fig.5D). Importantly, an Fgr small molecule inhibitor (TL02-59; with picomolar potency and strong specificity for Fgr [19]) induced similar behavioral shifts away from B3 (Figure 4C), altogether indicating that the global behavioral landscape is amenable to genetic and pharmacological intervention.

We then examined the therapeutic potential of targeting the Fgr-driven behavioral landscape in two models of acute inflammation. We first used a model of ischemia-reperfusion heart injury (modelling acute myocardial infarction; [11,20]), in which we obtained evidence of early vascular activation and damage manifested by release of Weibel-Palade bodies and vacuolation of endothelial cells that were dependent on neutrophils (Extended Data Fig.8C-E). Both endothelial damage and death of myocardial tissue after 1h of reperfusion were strongly reduced in mice lacking Fgr in leukocytes (generated by bone marrow transplantation; Figure 4D-E). We found similar myocardial protection in mice treated with the Fgr inhibitor either prior ischemia (Figure 4F), or given at the time of reperfusion (Extended Data Fig.8F). Although Fgr deficiency in our model was not restricted to neutrophils, we found that depletion of neutrophils prevented the beneficial effects of Fgr gene deletion (Extended Data Fig.8G) or inhibition (Extended Data Fig.8H), and that the TL02-59 inhibitor did not protect Fgr^{-/-} mice further (Extended Data Fig.8I), indicating that cardiac protection was through specific targeting of Fgr in neutrophils. Interestingly, infarcted Fgr mutants were also protected from long-term fibrosis (Extended Data Fig.8J). Thus, depletion or specific inhibition of the Fgr kinase confers strong protection from neutrophil-mediated inflammatory injury.

We finally used a model of acute kidney injury (glomerulonephritis) induced by low dose endotoxin combined with anti-glomerular serum [21] and Extended Data Fig.9A). This model featured accumulation of neutrophils in glomeruli and increased vascular permeability (measured by Evans blue extravasation; Figure 4G), as well as features of vascular occlusion (Extended Data Fig.9B), suggesting that glomerular vessels were primary targets of inflammatory injury in this model. Consistent with glomerular damage, two days after nephrotoxic serum treatment mice manifested strong alterations in protein and metabolite content in serum, and accumulation of proteins in urine (Figure 4H and Extended Data Fig.9C), all of which were completely prevented in the absence of hematopoietic Fgr (Figure 4H and Extended Data Fig.9C). Importantly, the protective effects seen in mice with Fgr deficiency did not compromise antimicrobial responses upon infection with Candida albicans or Staphylococcus aureus (Extended Data Fig.9D-E). Thus, Fgr (and possibly the other receptors and kinases identified in our screening as well) mediates the transition of intravascular neutrophils towards pathogenic behaviors (Extended Data Fig.9F) without affecting immune recruitment and anti-microbial defense, a finding that highlights the therapeutic value of targeting specific behavioral immune traits, rather than global immune activity.

Discussion

We have harnessed here two defining properties of live microscopic imaging, continued single cell tractability and focus on the native environment, to capture parameters of movement and shape of thousands of individual cells that enabled us to generate behavioral landscapes of active inflammation. We find that supervised selection of morpho-kinetic parameters guided by correlation networks aids in the description and identification of behavioral patterns in vivo. Development of new imaging and computational platforms will be critical to successfully implement behavioral analyses across multiple tissues and physiological contexts. This strategy allowed us to visualize and infer population dynamics in relevant physiological settings. Systematic measurement of tens to hundreds of these parameters per cell with high spatial and temporal resolution was key to identify combinations of parameters that faithfully scored leukocyte identities or states. In fact, our mathematical modeling predicted that, in some instances, individual parameters could score with almost perfect accuracy these immune properties. For example, sudden changes in movement (rather than speed itself) discriminated neutrophils from DCs in the infected trachea, while changes in cell compactness (i.e., track bounding boxes) discriminated macrophages from DCs, and cell shape, size and proximity to the endothelium identified pathology-associated neutrophils within inflamed vessels. The finding that parameters defining immune identities or states were often unexpected highlights the importance of capturing as many parameters as possible to faithfully report cell behaviors. Another corollary from these findings is that understanding the molecular determinants (genetic or signaling networks) underlying certain behaviors should shed critical information to uncover new drivers of disease. We show this to be feasible by screening for, and identifying, genes driving the transition towards pathogenic neutrophil states (B3 behavior), and by demonstrating that interfering with one of these genes (Fgr) prevents inflammatory injury. This was unexpected because Src-family kinases typically function redundantly to control multiple facets of myeloid cell activation [22], but agrees with the distinct role of Fgr in facilitating integrin activation downstream of PSGL-1 [23]. More importantly, it suggested that the behavior of inflammatory leukocytes within vessels is deterministic, a finding with major implications to target vascular inflammation without affecting antimicrobial immunity.

From an immunological perspective, a remarkable finding was that neutrophils transit between at least three clearly defined states within vessels, and that this is dictated both by environmental cues (e.g. presence of activated platelets [14]) and by cell-intrinsic properties (e.g. activity of Fgr and other receptors and kinases). These findings substantiate the distinct power of our "behavioromic" approach to describe innate immune cell dynamics and to identify relevant immune states in vivo. Our current analytical strategy is however improvable, and we foresee that the addition of new classes of parameters tractable by live imaging, including genetic reporters of cell fates [9], probes that report cellular biochemical reactions (e.g., production of reactive oxygen species, calcium flux or cell death; [24]), phagocytic activity and polarization [16], or even reporters of the cell's interacting history [25] will enormously enrich the value of the behavioral landscapes. Finally, we emphasize that while these behavioral landscapes lack the depth and molecular resolution provided by typical transcriptomic or proteomic profiling in non-dynamic biological settings, they could complement and even outperform them under highly dynamic scenarios, including areas of chronic vascular

inflammation [26], early activation of adaptive immunity in lymphoid organs [27], immune activity in the tumor microenvironment [28], or developmental stages in which transient cellular activities, rather than persistent lineage specification, dictate biological outcomes [29].

References

1. Papalexi, E. & Satija, R. Single-cell RNA sequencing to explore immune cell heterogeneity. *Nat. Rev. Immunol.* **18**, 35–45 (2018).

2. Sumen, C., Mempel, T. R., Bazo, I. B. & von Andrian, U. H. Intravital Microscopy: Visualizing Immunity in Context. *Immu* **21**, 315–329 (2004).

3. Lelkes, E., Headley, M. B., Thornton, E. E., Looney, M. R. & Krummel, M. F. The spatiotemporal cellular dynamics of lung immunity. *Trends Immunol.* **35**, 379–386 (2014).

4. Yamada, K. M. & Sixt, M. Mechanisms of 3D cell migration. *Nat. Rev. Mol. Cell Biol.* **20**, 738–752 (2019).

5. Goh, C. C. *et al.* Real-Time Imaging of Dendritic Cell Responses to Sterile Tissue Injury. *J. Invest. Dermatol.* **135**, 1181–1184 (2015).

6. Goh, C. C. *et al.* The impact of ischemia-reperfusion injuries on skin resident murine dendritic cells. *Eur. J. Immunol.* **48**, 1014–1019 (2018).

7. Lämmermann, T. *et al.* Neutrophil swarms require LTB4 and integrins at sites of cell death in vivo. *Nature* **498**, 371–375 (2013).

8. Winfree, S., Hato, T. & Day, R. N. Intravital microscopy of biosensor activities and intrinsic metabolic states. *Methods* **128**, 95–104 (2017).

9. Pittet, M. J., Garris, C. S., Arlauckas, S. P. & Weissleder, R. Recording the wild lives of immune cells. *Sci. Immunol.* **3**, (2018).

10. Adrover, J. M. *et al.* Programmed 'disarming' of the neutrophil proteome reduces the magnitude of inflammation. *Nat. Immunol.* **21**, 135–144 (2020).

11. Adrover, J. M. *et al.* A Neutrophil Timer Coordinates Immune Defense and Vascular Protection. *Immunity* **50**, 390-402.e10 (2019).

12. Chiang, E. Y., Hidalgo, A., Chang, J. & Frenette, P. S. Imaging receptor microdomains on leukocyte subsets in live mice. *Nat. Methods* **4**, (2007).

13. Woodfin, A. *et al.* The junctional adhesion molecule JAM-C regulates polarized transendothelial migration of neutrophils in vivo. *Nat. Immunol.* **12**, 761–769 (2011).

14. Sreeramkumar, V. *et al.* Neutrophils scan for activated platelets to initiate inflammation. *Science (80-.).* (2014) doi:10.1126/science.1256478.

15. Hasenberg, A. *et al.* Catchup: A mouse model for imaging-based tracking and modulation of neutrophil granulocytes. *Nat. Methods* **12**, 445–452 (2015).

16. Hidalgo, A. *et al.* Heterotypic interactions enabled by polarized neutrophil microdomains mediate thromboinflammatory injury. *Nat. Med.* **15**, (2009).

17. Mócsai, A., Walzog, B. & Lowell, C. A. Intracellular signalling during neutrophil recruitment. *Cardiovasc. Res.* **107**, 373–385 (2015).

18. Yago, T., Zhang, N., Zhao, L., Abrams, C. S. & McEver, R. P. Selectins and

chemokines use shared and distinct signals to activate β2 integrins in neutrophils. *Blood Adv.* **2**, 731–744 (2018).

19. Weir, M. C. *et al.* Selective Inhibition of the Myeloid Src-Family Kinase Fgr Potently Suppresses AML Cell Growth in Vitro and in Vivo. *ACS Chem. Biol.* **13**, 1551–1559 (2018).

20. García-Prieto, J. *et al.* Neutrophil stunning by metoprolol reduces infarct size. *Nat. Commun.* **8**, (2017).

21. Hirahashi, J. *et al.* Mac-1 (CD11b/CD18) links inflammation and thrombosis after glomerular injury. *Circulation* **120**, 1255–1265 (2009).

22. Futosi, K. & Mócsai, A. Tyrosine kinase signaling pathways in neutrophils. *Immunol. Rev.* **273**, 121–139 (2016).

23. Zarbock, A. *et al.* PSGL-1 engagement by E-selectin signals through Src kinase Fgr and ITAM adapters DAP12 and FcRγ to induce slow leukocyte rolling. *J. Exp. Med.* **205**, 2339–2347 (2008).

24. Specht, E. A., Braselmann, E. & Palmer, A. E. A Critical and Comparative Review of Fluorescent Tools for Live-Cell Imaging. *Annu. Rev. Physiol.* **79**, 93–117 (2017).

25. Pasqual, G. *et al.* Monitoring T cell-dendritic cell interactions in vivo by intercellular enzymatic labelling. *Nature* **553**, 496–500 (2018).

26. McArdle, S. *et al.* Migratory and dancing macrophage subsets in atherosclerotic lesions. *Circ. Res.* **125**, 1038–1051 (2019).

27. Mempel, T. R., Henrickson, S. E. & von Andrian, U. H. T-cell priming by dendritic cells in lymph nodes occurs in three distinct phases. *Nature* **427**, 154–159 (2004).

28. Boulch, M. *et al.* A cross-talk between CAR T cell subsets and the tumor microenvironment is essential for sustained cytotoxic activity. *Sci. Immunol.* **6**, 1–17 (2021).

29. Ivanovitch, K., Temiño, S. & Torres, M. Live imaging of heart tube development in mouse reveals alternating phases of cardiac differentiation and morphogenesis. *Elife* **6**, 1–30 (2017).

30. Lindquist, R. L. *et al.* Visualizing dendritic cell networks in vivo. *Nat. Immunol.* (2004) doi:10.1038/ni1139.

31. Faust, N., Varas, F., Kelly, L. M., Heck, S. & Graf, T. Insertion of enhanced green fluorescent protein into the lysozyme gene creates mice with green fluorescent granulocytes and macrophages. *Blood* **96**, 719–726 (2000).

32. Palomino-Segura, M., Virgilio, T., Morone, D., Pizzagalli, D. U. & Gonzalez, S. F. Imaging cell interaction in tracheal mucosa during influenza virus infection using two-photon intravital microscopy. *J. Vis. Exp.* (2018) doi:10.3791/58355.

33. Devi, S. *et al.* Neutrophil mobilization via plerixafor mediated CXCR4 inhibition arises from lung demargination and blockade of neutrophil homing to the bone marrow. *J. Exp. Med.* **210**, (2013).

34. Bauer, C. A. *et al.* Dynamic Treg interactions with intratumoral APCs promote local CTL dysfunction. *J. Clin. Invest.* **124**, 2425–2440 (2014).

35. Tran Cao, H. S. *et al.* Development of the transgenic cyan fluorescent protein

(CFP)-expressing nude mouse for 'technicolor' cancer imaging. *J. Cell. Biochem.* (2009) doi:10.1002/jcb.22128.

36. Çiçek, Ö., Abdulkadir, A., Lienkamp, S. S., Brox, T. & Ronneberger, O. 3D U-net: Learning dense volumetric segmentation from sparse annotation. in *Lecture Notes in Computer Science (including subseries Lecture Notes in Artificial Intelligence and Lecture Notes in Bioinformatics)* (2016). doi:10.1007/978-3-319-46723-8_49.

37. Welch, G. & Bishop, G. An Introduction to the Kalman Filter. *In Pract.* (2006) doi:10.1.1.117.6808.

38. Hao, Y. *et al.* Integrated analysis of multimodal single-cell data. *bioRxiv* (2020).

39. Venables, W. N. & Ripley, B. D. *Modern Applied Statistics with S Fourth edition by. World* (2002).

40. Bates, D., Mächler, M., Bolker, B. M. & Walker, S. C. Fitting linear mixed-effects models using lme4. *J. Stat. Softw.* (2015) doi:10.18637/jss.v067.i01.

41. Lloyd, S. P. Least Squares Quantization in PCM. *IEEE Trans. Inf. Theory* (1982) doi:10.1109/TIT.1982.1056489.

42. Henique, C. *et al.* Genetic and pharmacological inhibition of microRNA-92a maintains podocyte cell cycle quiescence and limits crescentic glomerulonephritis. *Nat. Commun.* **8**, 1829 (2017).

Author contributions:

Conceptualization: AH
Methodology: MP-S, FSC, AZ, TES, PLT, HCEW, OS, MMM, GFC, IGD, FDM, AH
Investigation: GC, MP-S, MMM, JS, DA, GFC, JLY, RM, JMA, AAC, SMS, ASV, SDC, MdP
Visualization: GC, MP-S, MMM, JS, DA
Funding acquisition: AH, FSC, PLT, LGN, GFC
Project administration: N/A
Supervision: PLT, SFG, TRM, AA-S, LGN, GFC, IGD, FDdM, AH
Writing – original draft: MP-S, AH
Writing – review & editing: All authors
Data and materials availability: All data, code, and materials used in the analysis are available to any researcher for purposes of reproducing or extending the analysis.
Competing interests. AH is a consultant for Flagship Pioneering. The authors declare no other conflicts of interest.

Materials & Correspondence. Requests should be addressed to Andres Hidalgo ahidalgo@cnic.es
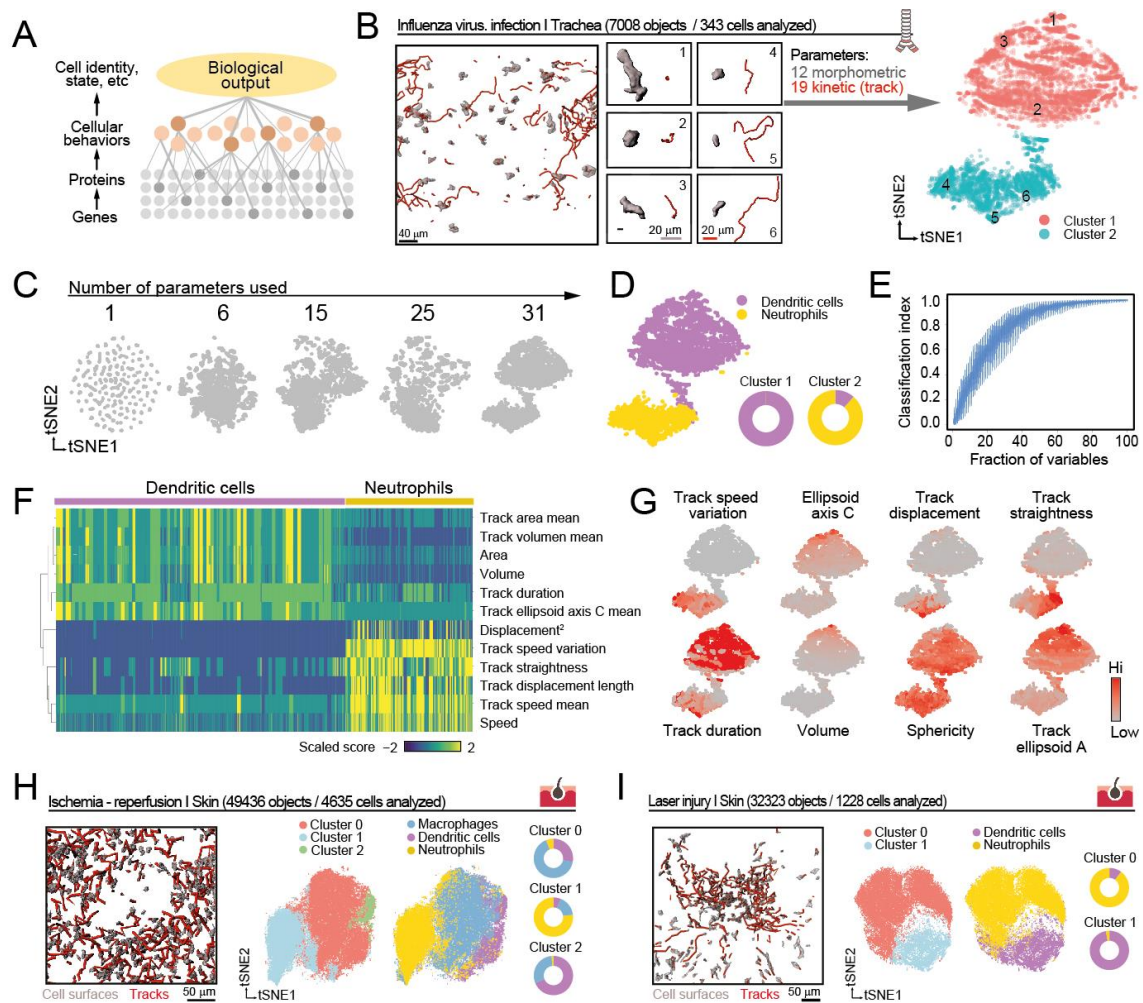
Figures and Figure legends

Figure 1. Behavioral maps capture immune identities. (A) Schematic showing the flow of biological information. Cellular behaviors captured by imaging integrate information from the molecular background of cells and can be used to describe higher-order biological outputs at the single cell level. (B) Representative 3D and track reconstructions of individual cells from images in tracheas infected with influenza. We obtained 31 morpho-kinetic parameters that we used to build bidimensional immune plots with the indicated cell number. We show 6 specific examples of cells that are localized in the tSNE plots at right by number codes. (C) The complexity and accuracy of plots representing cell behaviors are a function of the number of parameters used to describe the cells under analysis. (D) tSNE plot reconstruction of the data in (B) from two independent experiments, showing the distribution of neutrophils and DCs as defined by driver gene expression not included in the original analyses (see Methods). Donut plots at right indicate the degree of accuracy of behaviors in the two clusters compared with known lineages. (E) Qualitative stochastic model describing the change and variability in the level of knowledge of a biological system, here measured via a normalized classification index, as a function of the percentage of independent variables describing the system. (F) Heatmap of the differentially scored parameters for DCs and neutrophils. (G) Expression tSNE plots for the indicated parameters. (H) Representative 3D tracks and reconstructions, as well as the corresponding tSNE plots and donut plots, from images obtained in the skin during ischemia-reperfusion, or (I) the skin during laser-induced injury. Plots at left are by cluster, and at right by known cell types. The number of cells and all measured instants (objects) used in the analysis are indicated. Data are

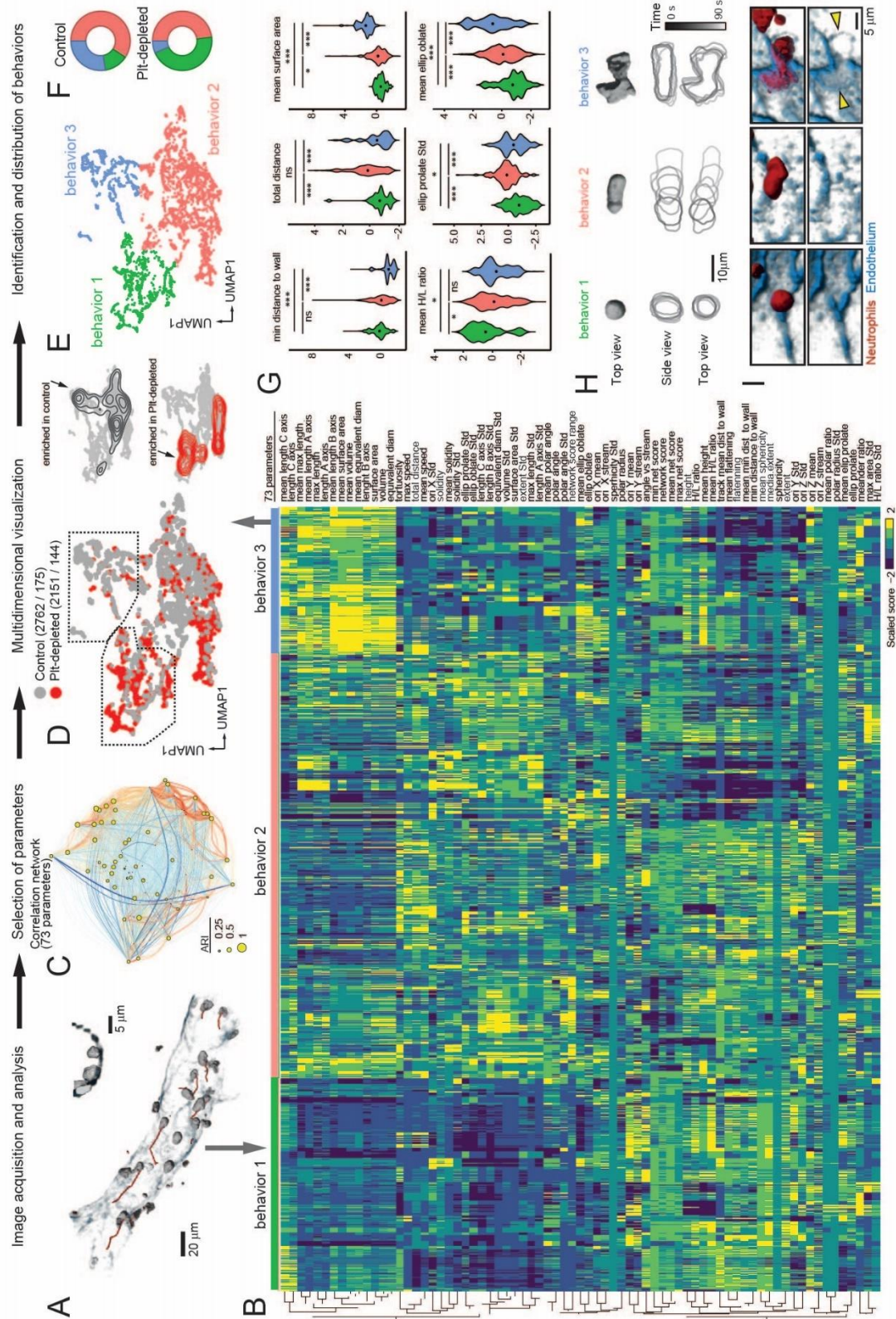from 3 independent experiments for each model. Spher., sphericity; Std, standard deviation.

Figure 2. Behavioral landscape of intravascular inflammation. (A) Representative 3D and track reconstructions of leukocytes inside an inflamed venule. Inset shows a cross-section of the vessel showing the localization and morphology of inflammatory leukocytes. (B) Heatmap of the dataset obtained for neutrophils inside inflamed venules

(TNFα) and all 73 morpho-kinetic parameters, distributed for the three identified behavioral profiles (1-3). (C) Correlation network of the dataset, showing parameters as nodes (circles) whose diameters are proportional to their Adjusted Rand Index (ARI), with lines connecting pairs of parameters colored according to positive (red) and negative (blue) correlations. The thicknesses of the links are proportional to the absolute value of the Pearson correlation coefficient for each pair. (D) tSNE representation of 4913 temporal cell reconstructions (319 cells) from control (grey) and platelet-depleted (red) mice. Density plots at right show the differential distribution of events for each group. Data are from at least 4 mice per group. (E) tSNE plot with the three distinct behavioral clusters labeled in colors, and the distribution of cells in each cluster for the control and platelet-depleted groups (F). (G) Distribution of cells from the three behavioral groups for the indicated parameters shown as violin plots. Data was analyzed using a univariate model (see Methods); *, $p<0.05$; ***, $p<0.001$; n.s., not significant. (H) Volumetric reconstruction of representative cells from behavioral clusters 1-3, as well as their temporal outline with temporal information. (I) 3D reconstruction of the same cells shown in (H), showing the distribution of an endothelial footprint (marked at both ends by arrowheads) only for cells with behavior 3. Ellip., ellipticity; Ori, orientation; H/L ratio, height to length ratio; Std, standard deviation.
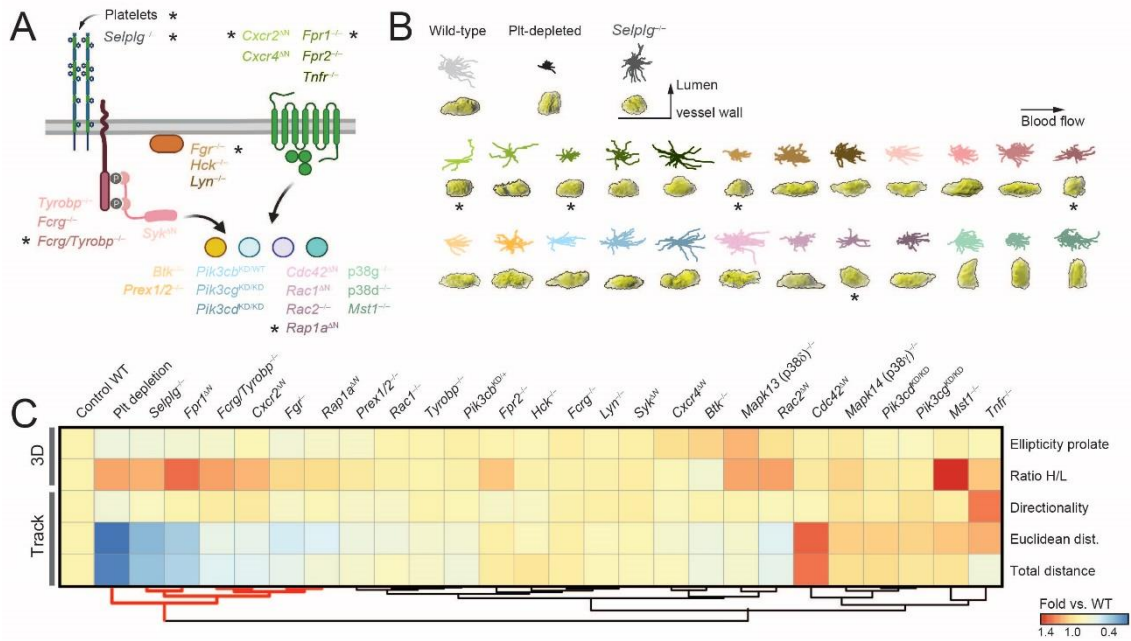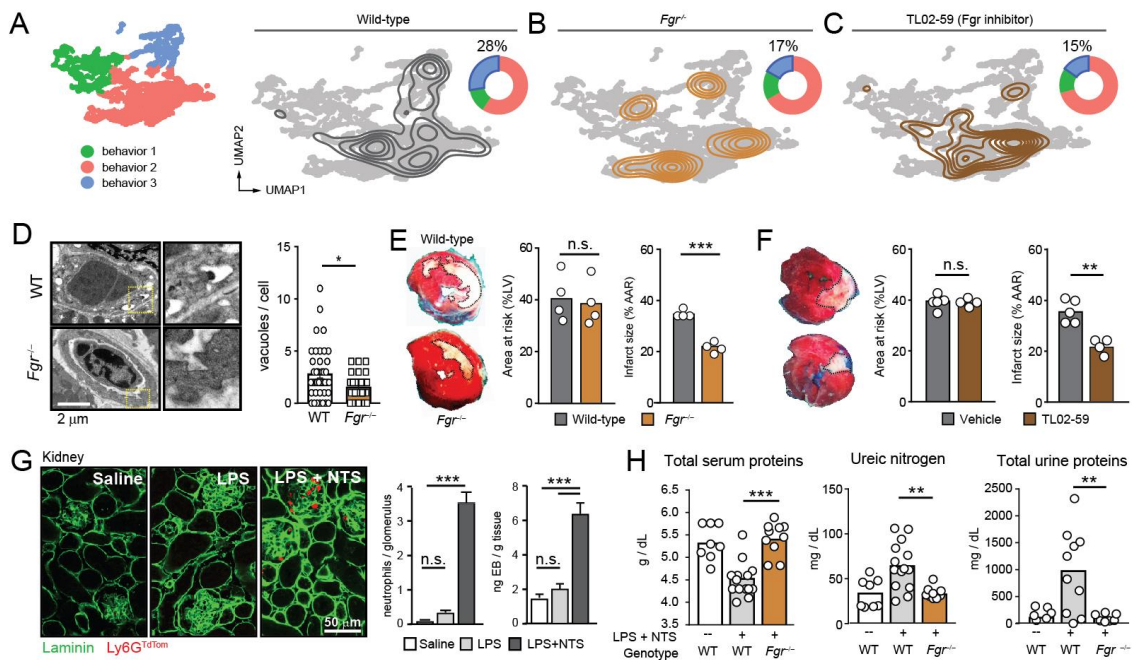
Figure 3. Screening for drivers of pathogenic intravascular behaviors. (A) Scheme of neutrophil signaling pathways indicating the genes analyzed here. Control, platelet-depleted and *Selplg*^{−/−} mice were used as reference groups in the behavioral screening. Asterisks denote mutants/conditions with behavioral changes similar to those of platelet-depletion and *Selplg*^{−/−} mice. (B) Representative 2D tracks and corresponding 3D morphologies for each condition/mutant, which are color-coded to match the genes shown in (A) including asterisks marking the same mutants as in (A). (C) Heatmap of relative changes over control for the 5 selected behavioral parameters (right), for all 24 mutants and 3 control groups, including platelet-triggered pathogenic activation through PSGL-1 (encoded by *Selplg*), which was used as reference for protection from inflammation. Individual analyses are shown in Figs.S6 and S7. Hierarchical clustering identifies 5 mutant behaviors that group together with platelet-depletion and *Selplg*^{−/−} groups (red lines below). Data is from 2093 cells for the track analyses, and 1643 for the 3D morphometric analyses from at least 3 mice per group and type of analysis.

Figure 4. Behavioral reprogramming protects from inflammation. (A) UMAP plot showing the distribution of the three behavioral groups (left), density plot for the wild-type control group layered over the global UMAP plot (right) and donut plot showing the distribution of cells among the three behavioral clusters. Similar UMAP and donut plots were built for *Fgr*$^{-/-}$ reconstituted mice (B), and mice treated with the Fgr inhibitor TL02-59 (C) to illustrate the shift of cells away from B3 after Fgr interference. Numbers in donut plots indicate the percentage of cells in B3. (D) Vascular damage in a model of myocardial ischemia and reperfusion determined by vacuolation of endothelial cells in hearts, from images obtained by transmission electron micrographs and quantified at right. Data from 2-3 mice and 28-43 areas analyzed. (E) Protection from myocardial injury in *Fgr*$^{-/-}$ mice, or wild-type mice treated with the inhibitor TL02-59 (F), after normalization to the areas at risk (AAR). Note the marked protection from infarct size, in both genetic and pharmacological models, relative to control mice, as shown in the heart sections for each group. The dead myocardial area is outlined in white in the heart sections. Data from 4-5 mice per group. (G) Glomerulonephritis model. Left, immunofluorescence of kidney tissue showing accumulation of neutrophils in glomeruli after injury induced by lipopolysaccharide (LPS) plus nephrotoxic serum (NTS) compared with saline or LPS alone. Right, quantification of neutrophils accumulated per glomerulus (from 3 mice and 80-153 glomeruli analyzed per group) and vascular damage measured by Evans Blue (EB) extravasation; data from 5 mice per group. (H) Analytics of serum and urine in control and glomerulonephritis-induced wild-type and *Fgr*$^{-/-}$ reconstituted mice. The control group was treated only with LPS; n= 8-12 mice per group. Data in D-G were analyzed by unpaired t-test, and one-way ANOVA with Tukey's multiple comparison test for (H). *, p<0.05; **, p<0.01; ***, p<0.001.

Extended Data

Behavioral immune landscapes of inflammation

Georgiana Crainiciuc, Miguel Palomino-Segura, Miguel Molina-Moreno, Jon Sicilia, David G. Aragonés, Jackson LiangYao Li, José M. Adrover, Alejandra Aroca-Crevillén, Sandra Martin-Salamanca, Alfonso Serrano del Valle, Heidi Welch, Oliver Soenhlein, Mariona Graupera, Fátima Sánchez-Cabo, Alexander Zarbock, Thomas E. Smithgall, Pierre-Louis Tharaux, Santiago F. González, Lai Guan Ng, Gabriel F. Calvo, Iván González-Díaz, Fernando Díaz-de-María and Andrés Hidalgo.

Correspondence to: ahidalgo@cnic.es

This PDF file includes:
> Extended Data Fig.1-10
> Materials and Methods
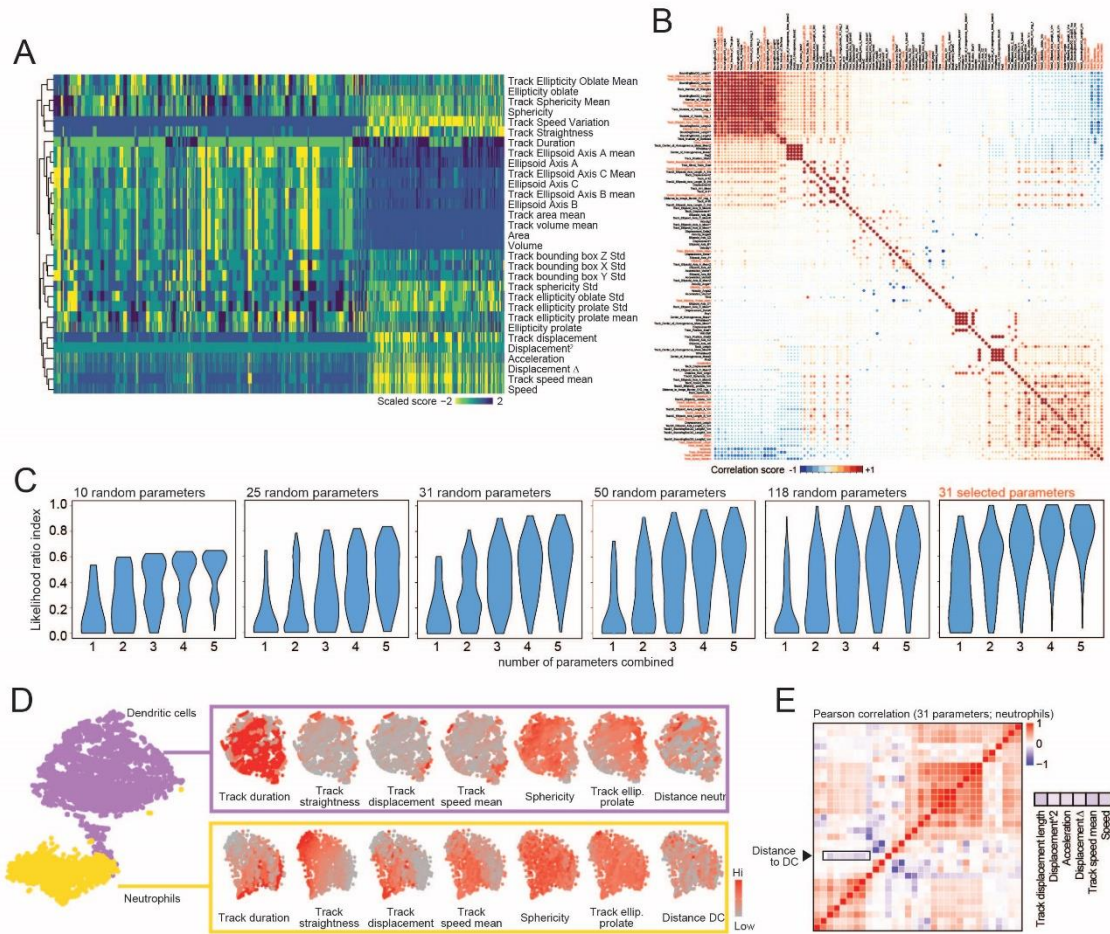> Captions for Movies S1 to S5

Other Supplementary Materials:
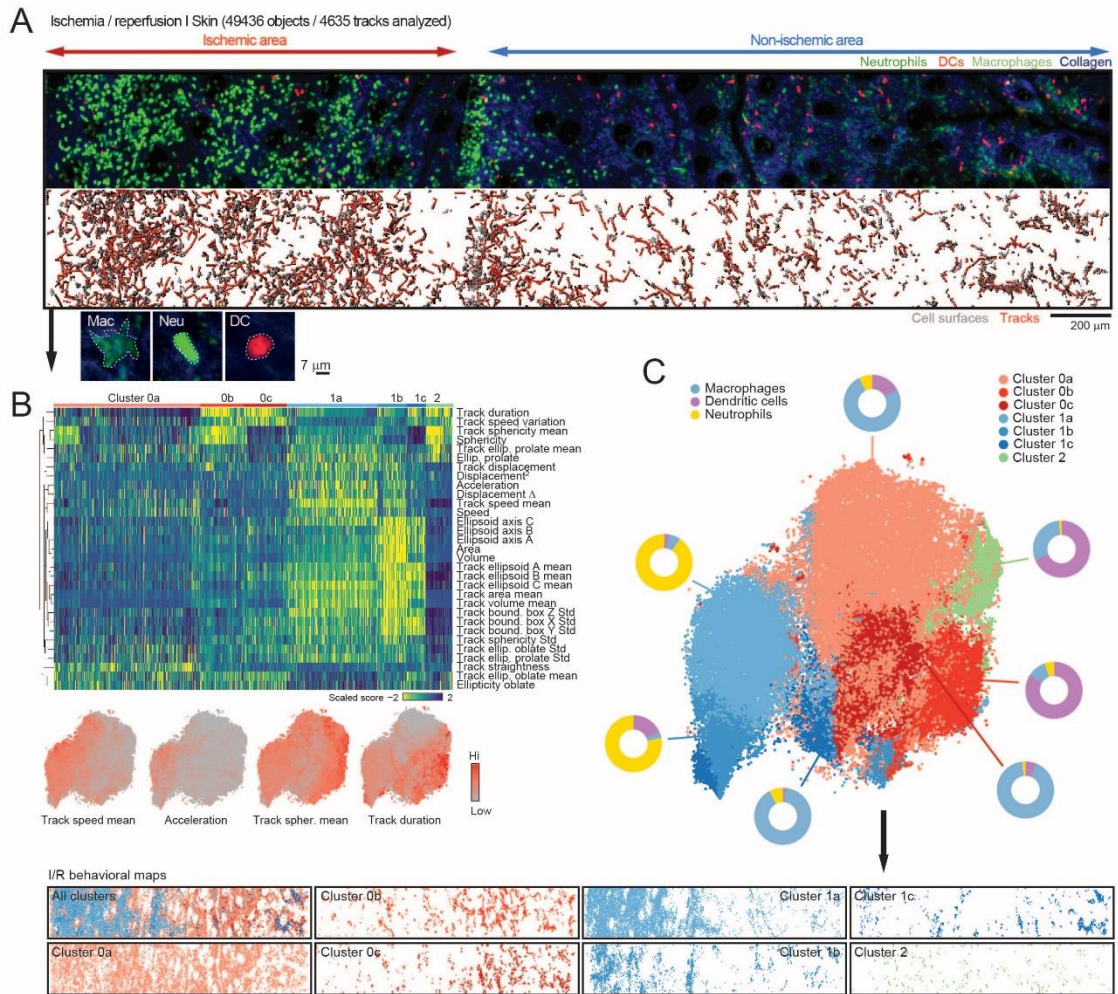> Tables S1 to S4
> Movies S1 to S5
> Data S1

Extended Data Fig.1. Selection of parameters for the behavioral analysis. (A) Workflow for the selection of parameters. 4D images are analyzed to extract morphometric and kinetic parameters (118 in our experiments using Imaris software). We performed supervised selection of the best features following criteria of redundancy, biological features of interest in the specific biological setup, or removal of non-biological parameters such as arbitrary position. In parallel we generated correlation networks for each experiment using those parameters (31 in the experiments reported here), and we visualized the distribution of the selected parameters in the correlation networks (see below). Finally, we reduced dimensionality using the selected parameters to identify behavioral clusters for further validation. For the "training" experiments shown here, where cell identities were known, we determined LRI/ARI to complement our correlation networks with the power of each parameter to classify cell correctly. The workflow is fully
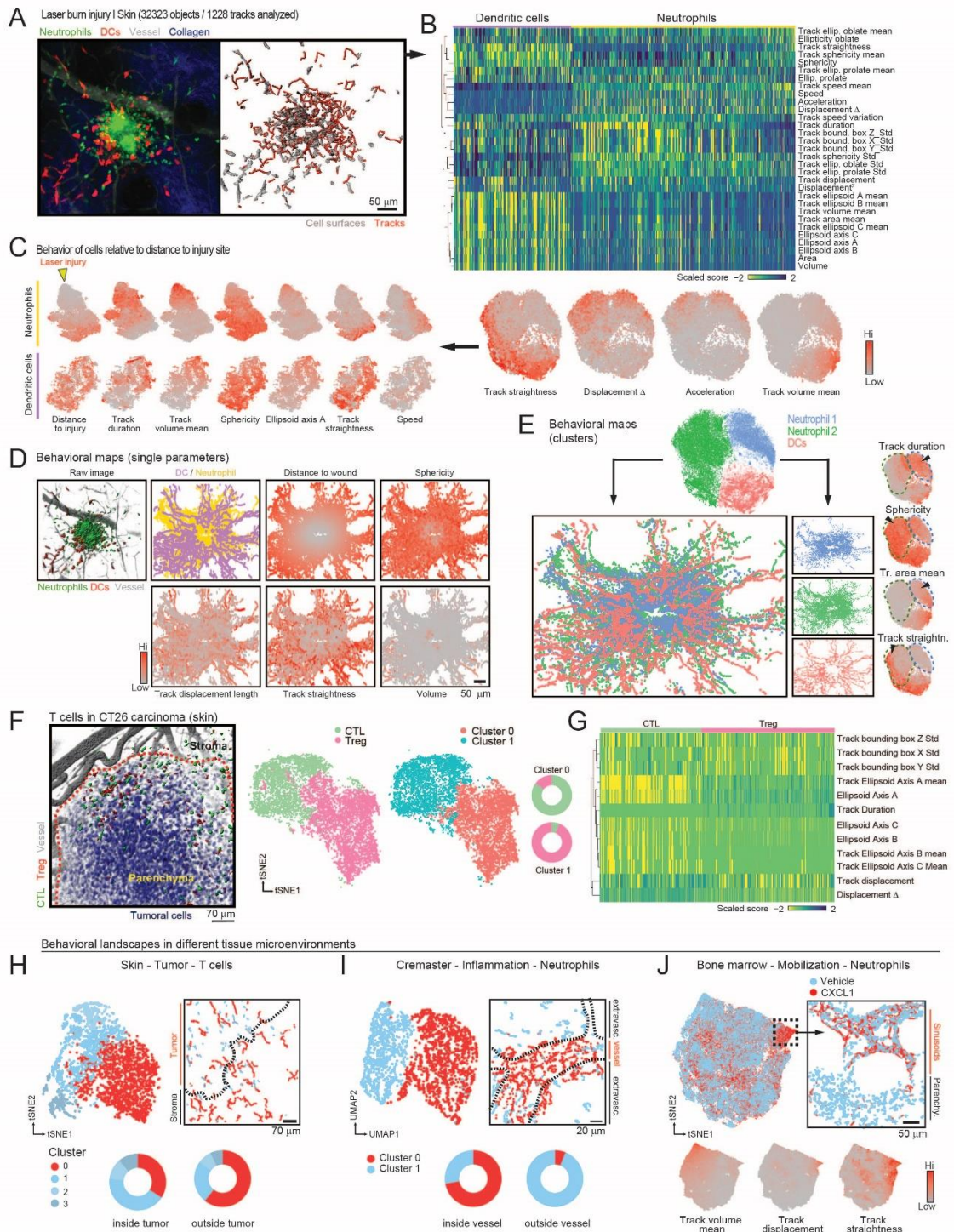
adaptable to other image analysis tools, as well as algorithms to establish correlation between parameters and for dimensional reduction, including Elastic net/Lasso regression methods. (B) Correlation networks used for the experiments shown in Figure1 with Imaris image analysis. Networks at left highlight the specific parameters used, identified by a number code used in Data S1. Right, correlation networks for the three datasets shown in Figure 1 (influenza infection in the trachea, ischemia-reperfusion in skin and laser injury in skin), showing parameters as nodes (circles) whose diameters are proportional to their LRI, as well as the positive (red) and negative (blue) correlations between each pair of parameters. The thickness of the links is proportional to the absolute value of the Pearson correlation coefficient for each pair, and the distance between parameters reflect the similarity of the Pearson coefficients with the rest of parameters. (C) Violin plots showing LRI/ARI values for all 118 vs. the selected 31 parameters. Lines represent medians. *, $p < 0.5$; **, $p < 0.01$ determined by Mann-Whitney non-parametric test. (D) Heatmap showing the LRI/ARI values for each of the 31 selected parameters for each experiment, as well as the Geometric mean for the three experiments combined, reflecting the consensus power of each parameter in our experiments. (E) tSNE plots generated by considering only the morphometric, or only the kinetic parameters, or both combined. The donut plots indicate the distribution of the analyzed cell types (macrophages, DCs and neutrophils) in each cluster. Note that the accuracy in identifying specific cell types for each cluster is always highest when both types of parameters are combined. (F) tSNE plots generated by considering all 118 parameters or only the selected 31 across all three experimental setups (influenza infection in the trachea, ischemia-reperfusion in skin and laser injury in skin). Note that cell classification per cluster was better for the selected 31 parameters. (G) tSNE plots showing the classification of cells into clusters by using all 118 parameters and a standard single cell analytical pipeline (Seurant_v4). Donut plots indicate the distribution of the analyzed cell types (macrophages, DCs and neutrophils) in each cluster.

Extended Data Fig.2. Behavioral landscape of the infected trachea. (A) Heatmap of the 31 behavioral parameters used for the trachea infection analysis. For a full list of all extracted parameters please refer to Data S1. (B) Pearson correlation matrix for all 118 parameters extracted from the trachea imaging experiment. (C) LRI (score of cell identities) are proportional to the number of parameters extracted from the imaging experiments and combined to infer identities. The violin plots show the distribution of LRIs when using 1-5 parameters to classify cells in the trachea experiment, assuming that only a set of 5, 25, 31, 50 or 118 parameters are available for analysis. Note that the LRI are shown here are for the full 118 parameter set, and are not comparable with the 31 subset of selected parameters, which feature higher LRI values, as shown in the violin plots at right. (D) Individual analyses of the behavior of DCs and neutrophils from the original dataset, shown as tSNE plots for each population. Each behavioral parameter can be visualized and compared across cell subsets and parameters to infer positive or negative correlations, as shown for *Distance to DC* which negatively correlates with cell speeds in the Pearson correlation matrix of the 31 parameters used in the final analysis (E).
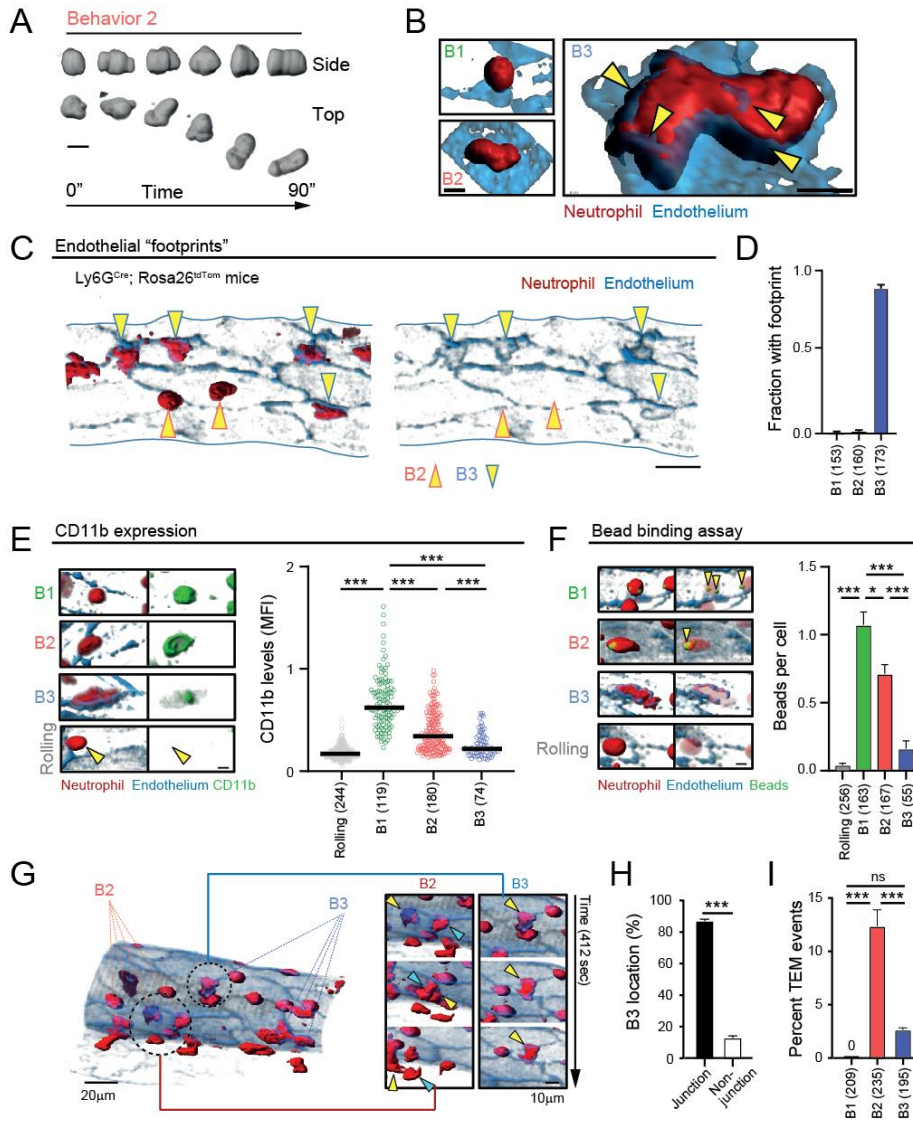
Extended Data Fig.3. Behavioral landscape of the skin under ischemia-reperfusion. (A) Representative image of I/R injury of the skin (original image on top; reconstruction of volumes and tracks at bottom). Below, examples of a typical GFP[lo] macrophage, a GFP[hi] neutrophil and an YFP+ DC used to classify the cells post-analysis. (B) Heatmap of all parameters and classified by cluster (0, 1 y 2) from the plot in Figure 1H, and further divided into subclusters shown in (C). Below, expression plots of selected parameters. (C) tSNE plot showing all subclusters identified in the heatmap in (B). Donut plots indicate the fraction of neutrophils, DCs and macrophages in each cluster. Bottom panels show the behavioral maps generated by back-gating each cluster into the original position for each cell so that maps show the position of cells with the same behavioral profile.
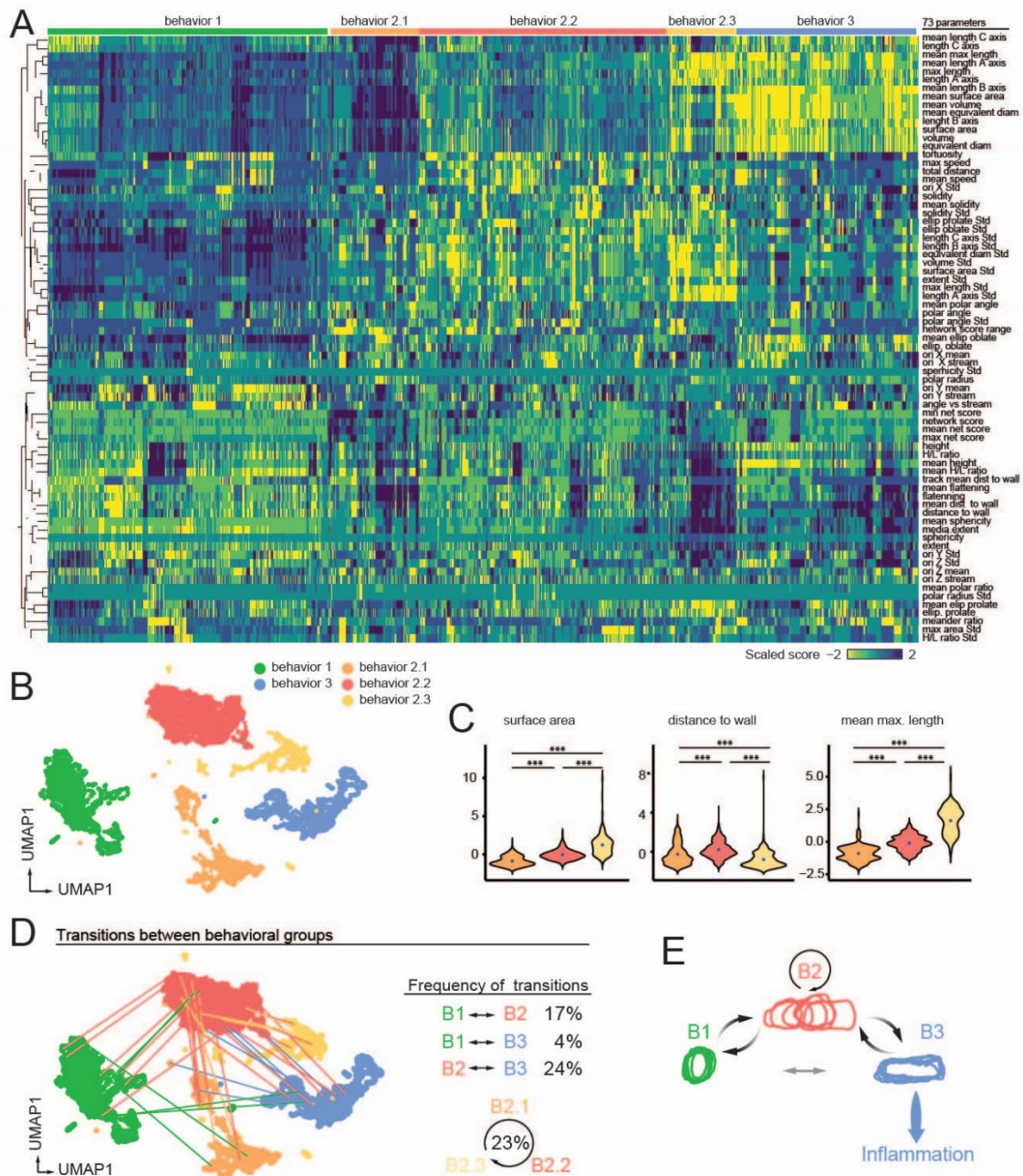
23

Extended Data Fig.4. Behavioral landscape of laser injury in the skin (A) Representative image of laser burn injury (original image left; reconstruction of volumes and tracks at right), (B) Heatmap of the all scored parameters, showing DCs and neutrophils. Expression tSNE plots of selected parameters are shown at bottom. (C) Individual analyses of the behavior of DCs and neutrophils from the original dataset, shown as tSNE plots for each population. Each behavioral parameterr can be visualized and compared across cell subsets and parameters to infer random or gradient distribution for each population. For example, the location of the laser injury can be extracted as a parameter (left, yellow arrowhead) that shows graded behaviors of neutrophils relative to their distance to the wound, but not for DCs. (D) Examples of

behavioral maps generated by projecting the intensity of specific parameters onto the XY location of individual cells at all time points. Actual image, plot-map by cell type and behavioral maps are shown. (E) Sub-clustering identifies two behavioral clusters of neutrophils and one for DCs (top), which were projected back onto their corresponding xyz position thus giving a profile of the distribution of behavioral clusters in the skin anatomy (middle). The neutrophil clusters feature differences in various parameters, as shown in the expression plots (arrowheads in the bottom tSNE plots). (F) Representative image of regulatory T cells (Treg) and cytotoxic T cells (CTL) in a CT26-induced tumor (red outline) in the skin, and tSNE plots of the cells classified by behavioral phenotype and by cell type. Donut plots show the match between both classifications. (G) Heatmap of the differentially scored parameters discriminating CTLs and Tregs. (H-J) Behavioral landscapes and maps of CTLs in carcinoma-bearing mice (H), neutrophils inside or outside inflamed vessels (I), and bone marrow neutrophils before and after mobilization with CXCXL1 (J). Donut plots and expression plots illustrate the correlation between behavioral patterns or parameters and their localization in tissues. Dashed lines in the behavioral maps in (H-I) delineate tumor-stroma or vessel-parenchyma borders, respectively. Data are from one experiment per condition to distribution of cells in a single anatomical area.
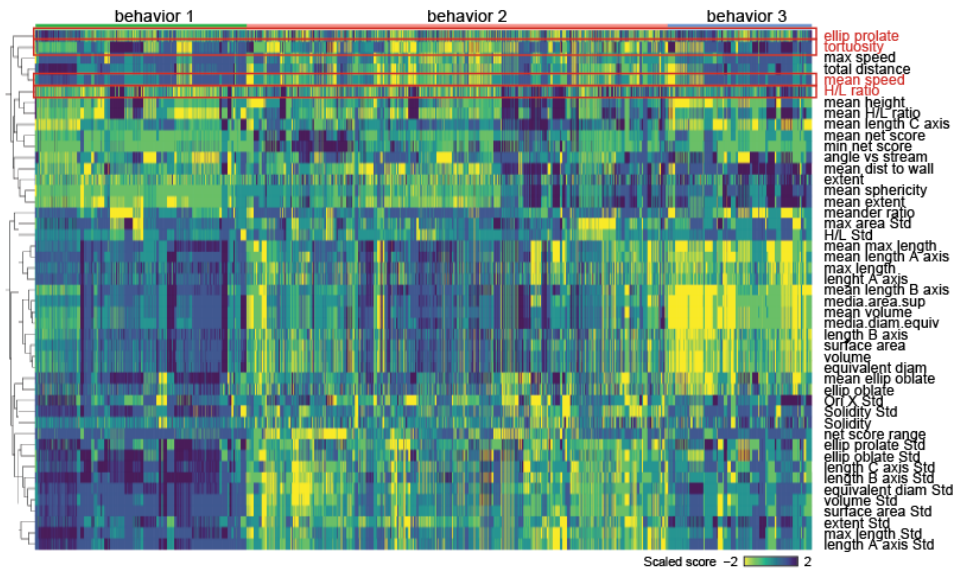
Extended Data Fig.5. Neutrophil states inside inflamed venules. (A) Rapid changes in morphology for neutrophils in the B2 group, following inchworm-type crawling during a 90 sec recording; scale bar, 10 μm. (B) Membrane extensions (yellow arrowheads) forming around large oblate neutrophils in the B3 group, but not from B1 or B2; scale bar, 5 μm. (C) Representative micrograph of an inflamed vessel from Ly6G^Cre; Rosa26^tdTom mouse with several neutrophils exhibiting B2 and B3 behavioral profiles (arrowheads), and "footprints" beneath B3 cells; scale bar, 10 μm. The presence of the footprints for each behavior is quantified in (D). (E) Micrographs and quantification of CD11b expression measured by in vivo imaging across the different behavioral groups, with rolling neutrophils included as reference cells; data from 6 mice. (F) Micrographs and quantification of the number of beads phagocytosed by neutrophils from each behavioral group, including rolling cells; scale bar, 5 μm. (G) Representative 3D image of an inflamed cremaster vessel showing examples of B2 and B3 neutrophils (left image), which were examined for extravasation across the endothelial wall over time (arrowheads in insets, right). (H) Percent of B3-type neutrophils that localize in junctional vs. non-junctional areas, and (I) the frequency of transendothelial migration (TEM) for each behavioral group of neutrophils. Data is from the indicated number of cells per group from 5 mice. Bar graphs show mean ± SEM and data were analyzed by one-way ANOVA with Tukey's multigroup comparison test (F, I) or unpaired t-test (H). Number of cells per group from 3-5 mice each are indicated in brackets.
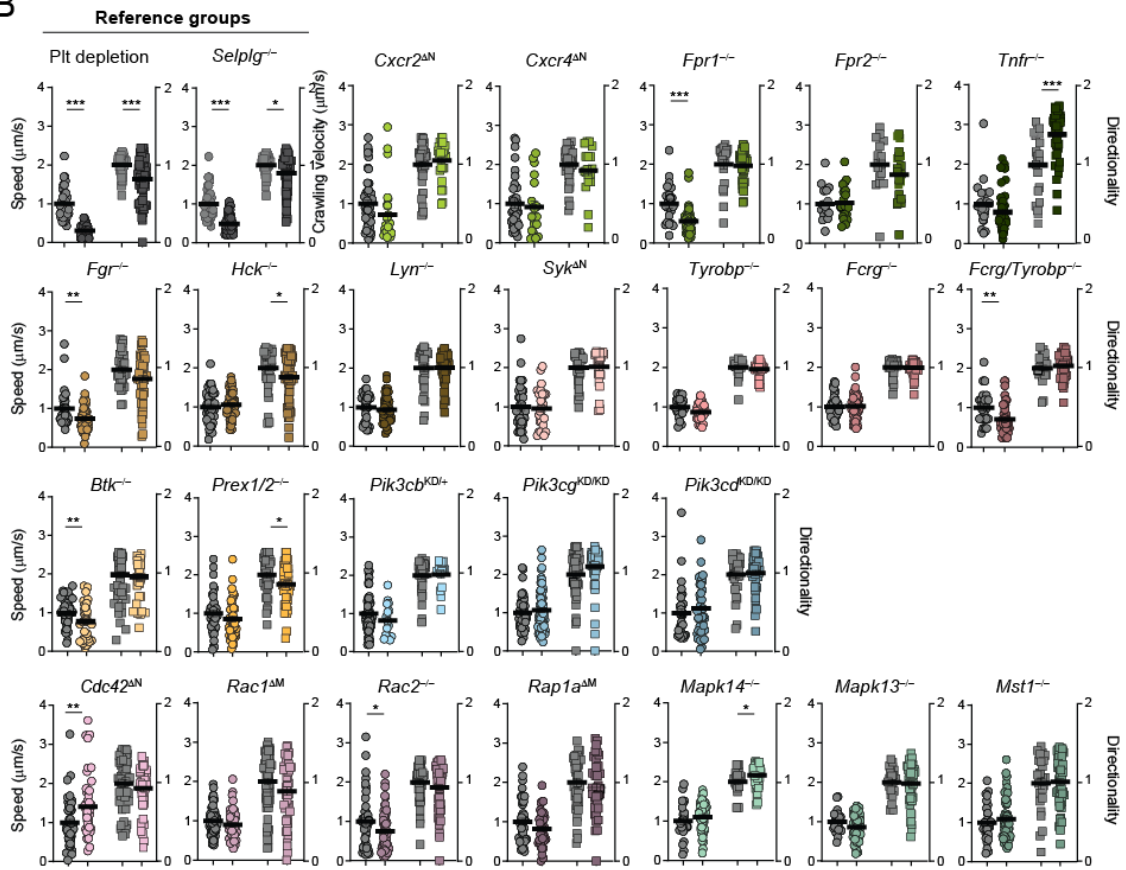
26

Extended Data Fig.6. Transitional states of neutrophils in vessels. (A) Heatmap of all parameters across all behaviors, including the three sub-groups in B2. (B) UMAP based on hierarchical clustering to identify two additional behavioral clusters within B2. (C) Distribution of cells in each sub-cluster B2.1, B2.2 and B2.3 for the indicated parameters, showing for example that cells B2.3 feature sizes and distances to the vessel wall similar to those of B3. (D) Transitions between behavioral clusters shown graphically in the UMAP (left) and quantified at right. (E) Scheme illustrating the most common transitions typically involving passage through B2, suggesting that this is an obligate transitional stage for neutrophils in inflamed vessels. Drawings in each group represent the silhouettes of representative cells at different times as in Figure 2H.
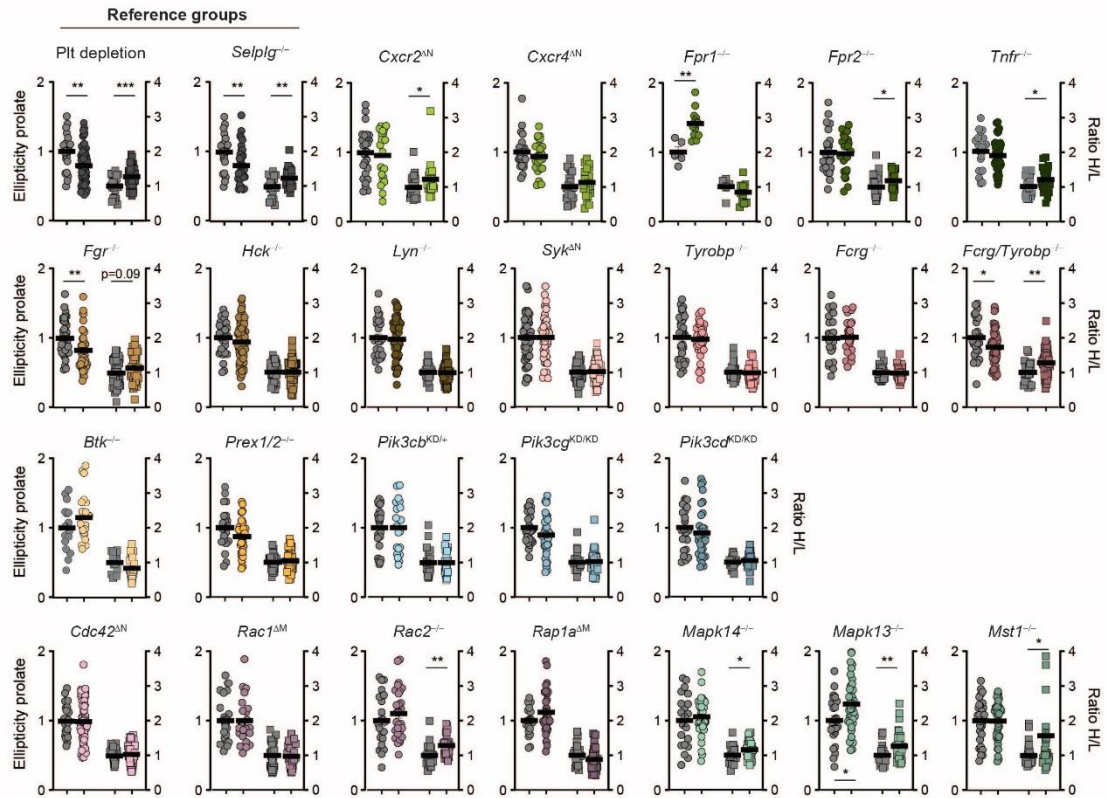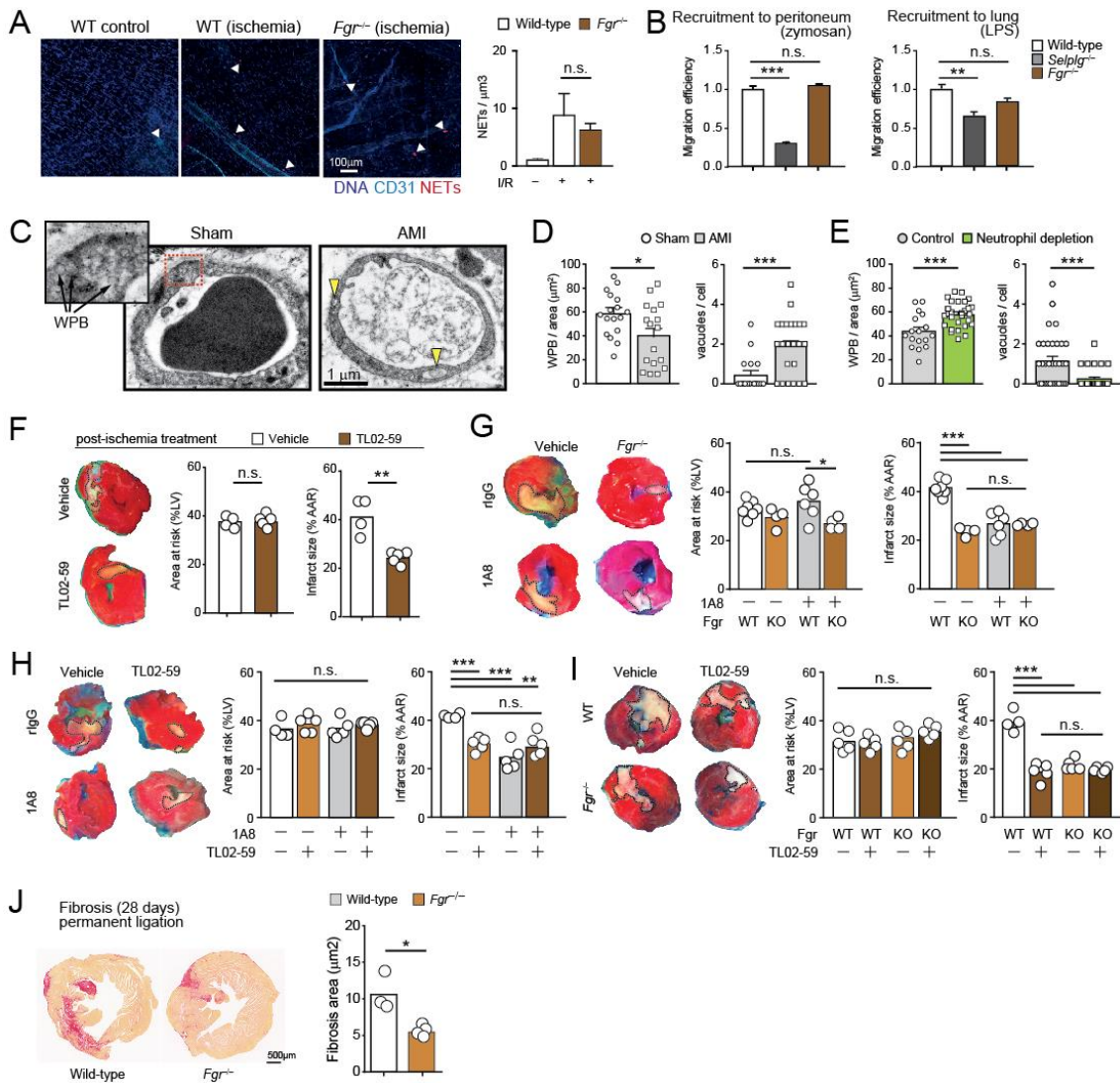
Extended Data Fig.7. Track parameters in the behavioral screening. (A) Heatmap of the differentially scored behaviors among the three main behavioral groups (B1, B2 and B3). Outlined in red are the specific behaviors chosen for our screening in Figure 3. Note that "tortuosity" is an inverse measure of "directionality", which was used in our screening. (B) Speed and directionality obtained by epifluorescence (2D) analysis of cremasteric venules in mice with mixed chimeric bone marrow of wild-type[DsRed] and non-fluorescent mutant donors, which provided internal controls for each group. Data are from 16-71 cells per parameter and mutant, and thick lines represent means, *, $p<0.05$; **, $p<0.01$; ***, $p<0.001$ as determined by unpaired t-test analysis.

Extended Data Fig.8. Morphometric parameters in the behavioral screening. Ellipticity prolate and H/L ratios measured for individual cells in static 3D reconstructions from 24 mutant and 3 control groups as summarized in Figure 3. Values are from cremasteric venules in mice with mixed chimeric bone marrow of wild-type[DsRed] and non-fluorescent mutant donors, which provided internal controls for each group. Data are from 5-88 cells per parameter and mutant, and thick lines represent means, *, p<0.05; **, p<0.01; ***, p<0.001 as determined by unpaired t-test analysis.
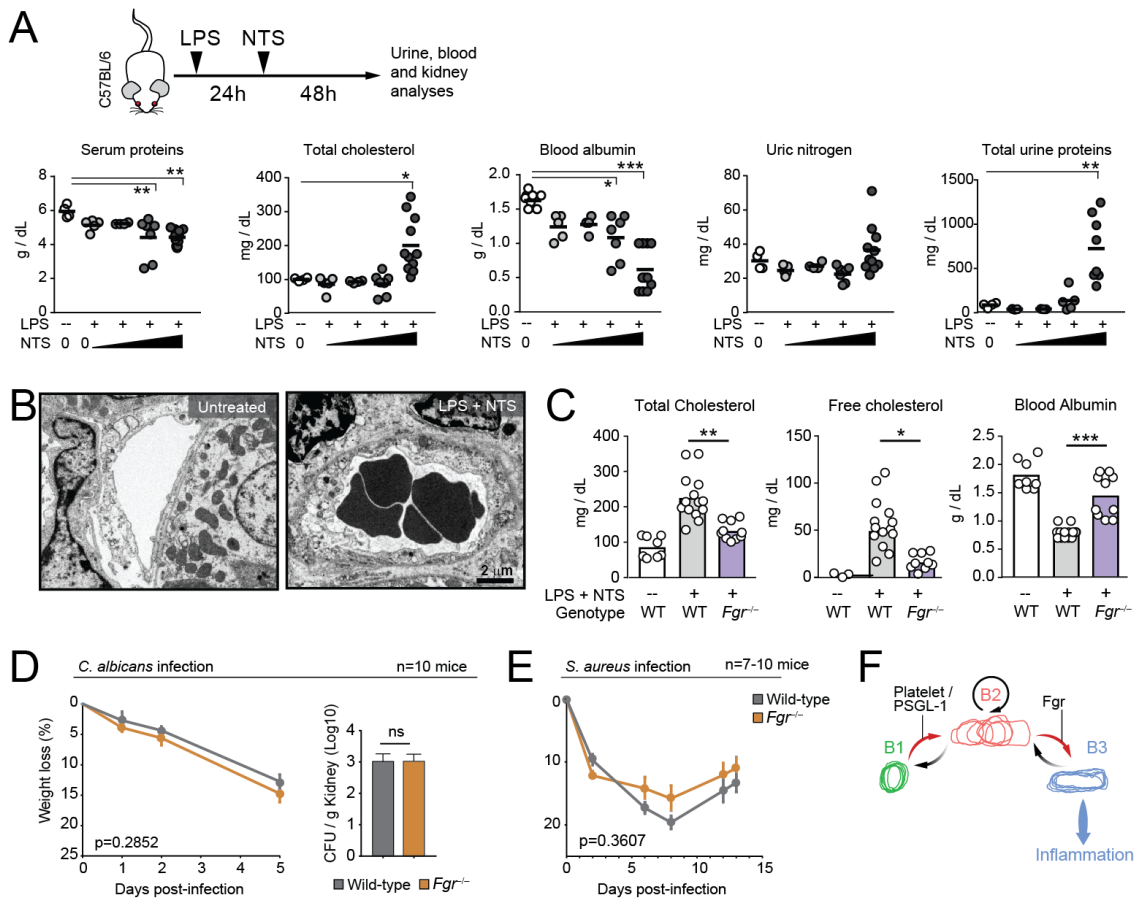
Extended Data Fig.9. Protection from myocardial injury by targeting Fgr. (A) Micrographs of NETs (positive for citH3 and MPO; red) and vessels (blue) in cremasteric venules of wild-type subjected or not to I/R, and *Fgr*−/− mice subjected to I/R. Right, quantification of NETs per tissue volume; Data is from 3 mice per group. (B) Competitive recruitment of wild-type and *Fgr*−/− neutrophils to the peritoneum after zymosan injection (n=5-12 mice), or to the bronchoalverolar lavage of lungs after LPS instillation in mixed chimeric mice (n=4-10). *Selplg*−/− neutrophils are shown for comparison of impaired migration. Values are normalized to reference wild-type competitors across the different groups and given as migration efficiencies. (C) Micrographs of Weibel-Palade bodies (WPB) and vacuoles in myocardial vessels after sham or ischemic challenge, which are quantified in (B). These measures of vascular damage are dependent on neutrophils, as shown after experimental depletion with 1A8 antibody (C). Data are from 2 mice and 17-29 images. (D) Effect of the Fgr antagonist TL02-59 in myocardial death upon ischemia-reperfusion, when given after ischemia at the time of reperfusion. Micrographs of heart sections at left illustrate the protective effect on myocardial death (outlined whitish regions). Data are normalized to the area at risk (AAR) and are from 4 mice per group. (E) Combination of neutrophil depletion with 1A8 antibody, and Fgr deficiency in transplanted mice. The infarcted areas are normalized with the areas at risk. Data are from 4-7 mice per group and analyzed by one-way ANOVA with Tukey's multiple comparisons test. (F) Combination of neutrophil depletion with the Fgr agonist TL02-59. Data are from 4-5 mice per group. (G) Combination of the Fgr inhibitor in hematopoietic

Fgr$^{-/-}$ mice, with no effect in further protecting from myocardial death. Data from 4-5 mice per group. (H) Myocardial fibrosis (left ventricle) determined by hematoxylin and eosin staining in control wild-type and *Fgr*$^{-/-}$ mice subjected to permanent ischemia and analyzed after 28 days. The fibrosis area is represented at right. Data from 3-4 mice per group. Data from (A-B) was analyzed by one-way ANOVA with Tukey's multiple comparison test; (G-I) was analyzed by two-way ANOVA with Tukey's multiple comparisons test. All other panels are compared by unpaired-t test (C-F and J).

Extended Data Fig.10. Protection from nephrotoxic injury by targeting Fgr. (A) Schematic of the nephrotoxic injury model (top) and setup of conditions combining endotoxin (LPS) with increasing amounts of nephrotoxic serum (NTS), resulting in gradual increase in markers of kidney damage in serum and urine. Data from 4-11 mice per dose. (B) Transmission electron micrograph of kidney venules showing an example of intravascular occlusion in the NTS-treated mice, from 2 mice and 25-30 images analyzed. (C) Levels of the indicated metabolites in plasma of control and *Fgr*^{-/-} mice before and after induction of glomerulonephritis with LPS plus NTS. The control group was treated with LPS only.; data is from 7-14 mice per group. (D-E) Mice reconstituted with marrow from wild-type or *Fgr*^{-/-} donor mice were infected with *C. albicans* (D) or *S. aureus* (E) and infection progression was measured by weight loss, and in the case of C. albicans infection by scoring the fungal load in kidneys (CFU). Data in (A) was analyzed by unpaired t-test. For (D-E) groups were compared by two-way ANOVA analyses for weight loss, and unpaired t-test for CFUs. Data in (C) was analyzed by one-way ANOVA with Tukey's multiple comparisons test. (F) Scheme modeling neutrophil states, transitions, and delivery of inflammatory signals to the host tissues from B3 cells. Each transition is proposed to be caused by different signals, e.g. delivered by platelets and PSGL-1 for initial transition from B1 to B2, and via Fgr for transitions from B2 to B3.

Supplementary information

Materials and Methods

Mice

We performed all experiments in 7–18-week-old male C57BL/6 wild-type, CD11c[YFP] [30] LyzM[GFP] [31] and Ly6G[Cre]; Rosa26[tdTom] [15] reporter mice. Reporter knock-in lines were used in heterozygosis to prevent gene deletion. All mice were bred in the C57BL/6 background. Mouse lines used in the in vivo screening using bone marrow transplantation are listed in Table S1. For neutrophil depletion, we injected 50 µg of anti-mouse Ly6G antibody (clone 1A8 from BioXcell; West Lebanon, NH, USA) intravenously at 24 and 48 hours prior analyses, resulting in >93% reduction in blood neutrophil counts compared with vehicle controls. For platelet depletion, we treated mice i.p. with 50 µl rabbit anti-platelet serum (Accurate Chemical; Westbury, NY) diluted in 200 µl of PBS 24 hours before the experiment with >95% depletion efficiency. To inhibit Fgr, we treated mice intravenously with 100 µg of the specific inhibitor TL02-59 [19] diluted in saline 2h prior experimentation. Mice were housed in a specific pathogen-free facility at Centro Nacional de Investigaciones Cardiovasculares (CNIC) under a 12 h light/12 h dark schedule (lights on at 7:00, off at 7:00), with water and chow available ad libitum. All experimental procedures were approved by the Animal Care and Ethics Committee at CNIC and regional authorities.

4D Two-photon intravital microscopy (2PIM)

We performed 2PIM imaging in three different models of inflammation: influenza-infection of trachea, ischemia-reperfusion (I/R) of and laser burn injury of skin. The trachea model was performed exactly as reported [32]. For the skin models, we reprocessed raw data from our published data on ischemia-reperfusion [6] and laser-induced heat injury [6] which used LyzM[GFP]; CD11c[YFP] mice. For analyses of bone marrow neutrophils before and after CXCL1 treatment we used 4D imaging datasets from [33], and for Tregs and CTLs in CT26 tumor-bearing mice from [34]. The files obtained for analysis are therefore a collection of new and existing 4D intravital imaging experiments using the settings and workflow indicated in Table S2 and Table S3.

For two-photon imaging of influenza-infected trachea, we inoculated CD11c[YFP] mice with influenza virus strain PR8 (A/PR/8/34) 3 days before imaging as previously described [32]. Briefly, we adoptively transferred 5 x 10^6 neutrophils isolated from bone marrow of CK6[ECFP] [35] to the infected CD11c[YFP] mice 12 h before imaging. At the time of imaging, we anesthetized infected mice with a mix of ketamine (100 mg/kg bodyweight, Parke Davis) and xylazine (10 mg/kg bodyweight, Bayer) followed by surgical exposure and cannulation of the trachea in a customized two-photon platform (TrimScope, LaVision BioTec, Bielefeld, Germany). We acquired full Z stacks of 40 µm every 30 seconds for 30 minutes to generate 4D images using a customized upright two-photon platform (TrimScope, LaVision BioTec). Two-photon probe excitation and tissue second-harmonic generation (SHG) were obtained with a set of two tunable Ti:sapphire lasers (Chamaleon Ultra I, Chamaleon Ultra II, Coherent) and an optical parametric oscillator that emits in the range of 1,010–1,340 nm (Chamaleon Compact OPO, Coherent), with output wavelength in the range of 690–1,080 nm.

In vivo live imaging of skull bone marrow neutrophils was performed as described in [33]. Briefly, LyzM[GFP] mice were anesthetized and skin covering the skull was removed to expose the imaging area. The exposed skull was superfused with PBS and immobilized under a custom-made stage for multiphoton microscopy (LaVision TriM Scope II) with a 20X 1.4 NA WI objective (Olympus). Steady state time lapse videos were taken at 20

second intervals for approximately 10 minutes, before 100 ng of recombinant CXCL1 (KC) in PBS (R&D Systems, cat. no. 453-KC) was injected subcutaneously, and mice skulls were imaged using the same settings post-treatment to follow the effects of KC administration.

Spinning-disk intravital imaging of the cremaster muscle
We used 2D (epifluorescence) and 3D imaging analyses (spinning-disk) for the genetic screening as this did not demand generation of fluorescent reporters for each mutant line, and 4D analyses for the full behavioral analyses in the *LyzM*^{GFP} or Ly6G^{Cre}; R26^{tdTom} reporter lines. We performed intravital imaging of the cremaster muscle after TNF-α stimulation (R&D Systems, 0.5 µg, intrascrotal injection) as previously reported [11,14] using the VIVO system (Intelligent Imaging Innovations, Denver, CO). We used a plan-Apochromat 40x W NA1.0 ∞/0 objective (Zeiss) and the SlideBook software (Intelligent Imaging Innovations) for image acquisition. For the 2D motility analysis of mutant neutrophils in mixed chimeric mice, we analyzed 6-10 venules per mouse 120 to 180 min after TNF-α treatment by epifluorescence imaging (Cy3/561 channels for PE, FITC/488 channels for FITC and Cy5/640 channels for APC) and bright-field images with 2×2 binning with a 3 s interval for 2 min on each field of view. For the morphological analysis of the mixed chimeric animals, we generated 3D confocal reconstructions using laser stacks for 488, 561 and 640nm beams coupled with a confocal scanner (Yokogawa CSUX-A1; Yokogawa, Japan) and images were acquired at 0.5 µm Z-intervals. For double staining with phycoerythrin (PE)- and FITC-conjugated antibodies, acquisition was facilitated by single (FITC) and quadrant (PE) filters to avoid bleed-through of fluorescent signals between channels. For the visualization of leukocytes, 10 min before imaging we injected intravenously 1.25µg per mouse of fluorescently labeled anti-Ly6G-APC and anti-CD62L-FITC and in some instances 0.5µg anti-CD41-PE to visualize platelets. For 4D intravital imaging, we analyzed 6-10 venules per mouse 120 to 180 min after TNF-α treatment using laser stacks for 488, 561 and 640nm beams coupled with a confocal scanner (Yokogawa CSUX-A1; Yokogawa, Japan). We acquired full Z stacks that covered a similar cylindrical segment of the venules with an average depth of 26 µm with 1-2 µm Z-intervals for a total period of approximately 8 minutes (see full settings in Table S2). For the visualization of the vessel wall, we injected 1.4ug fluorescently labeled anti-CD31-APC in combination with TNF-α as published [13]. For the characterization of the CD11b expression levels of intravascular neutrophils, we injected 3ug of fluorescently labeled anti-CD11b-FITC (clone M1/70; BD Biosciences) 10 min prior imaging. For the in vivo bead binding assay, we incubated red FluoSphere™ sulfate beads (1 µm diameter; excitation/emission of 580/605 nm, respectively; Thermo Fisher) with 1 mg/ml bovine serum albumin for 2h in phosphate-buffered saline. Immediately before use, we sonicated the beads for 15 min in a water-bath sonicator. Albumin-coated fluospheres (10^9) were intravenously injected into mice prepared for intravital microscopy 10 minutes prior imaging, as published [16].

Image analysis
We processed and corrected the newly-generated and existing datasets by performing drift correction and channel unmixing using custom scripts (Python 3.5) and FIJI. For the trachea experiments we additionally generated new imaging channels specific for the cells of interest using the 'Coloc' functionality of Imaris (Oxford Instruments, 9.5.1). We then performed cell detection, volumetric reconstruction ('objects´), object filtering by voxel size (removing objects <40 voxels) and tracking, using Imaris. Analyzed videos

were exported as .csv files containing all the raw values and statistical parameters for each detected object and track, and aggregated using custom Python scripts. All channel-related parameters were removed from the list and the remaining 118 parameters used for further curation. Where relevant, we also calculated the standard deviations 'variation' parameters, which were calculated for time series data by dividing the parameter's standard deviation by its mean value by scripting. Finally, to facilitate "back-gating" analysis, whereby identified subpopulations (e.g. from tSNE plots) can be referenced back to the imaging data, we maintained the original Imaris surface identifiers throughout the whole data analysis workflow, and these surfaces could be isolated using custom Python-based scripts compatible with Imaris XTensions functionality. All parameters using Imaris, and their contribution to cell classification, are listed in Excel format in Data S1 file.

For image analyses of the cremaster muscle, we generated our own analytical method for intravascular neutrophils called Automated Cell Migration Examination (ACME). ACME was designed to perform automatic feature extraction for migrating cells, including automatic detection, segmentation and tracking of cells within vessels. Automated analysis with ACME increased the number of cells that could be analyzed by an order of magnitude relative to manual annotation and reduced bias. For ACME we combined deep learning and machine learning blocks to segment, track and extract features from cells moving within blood vessels. ACME implements the following sequential processing pipeline: first, each 3D temporal instant in a 4D volume is fed into the 3D dual segmentation system, based on a strongly-regularized 3D U-Net CNN (Convolutional Neural Network) [36], which was trained using functions specifically designed to address challenges in vessels (cylindrical structures), including high class imbalance between background, vessel wall and cell classes, strong data variability and to improve precision. This module generated a mask outlining the area of the 3D block corresponding to the blood vessel, a set of masks containing the regions likely to be cells, and for each region a value that quantifies the probability of a region to be a cell. In a second step, the 4D cell volumes were passed to a 3D tracking system. This module evaluated the temporal sequence of segmented regions and generated the trajectories in a multi-object tracking scenario and handled collisions between cells. This module was based on a three-pass 3D Kalman-filter tracking system [37], which is complemented in the first and second passes with collision detection and morphological post-processing modules, respectively. With information of the trajectories, blood vessel and cell segmentations, the feature extraction module represented the cell dynamics within a short temporal window around each time instant, to generate "short-term cell features". Short-term features are formed by aggregating two types of features: instantaneous features, related to the position and shape of cells in each time instant (i.e. objects); and dynamic features, representing the evolution of these instantaneous variables in the temporal window as well as other features related to the trajectory of each cell (referred here as tracks). Finally, the last step is a cell selection module which was based on these short-term features and applied filters that aligned with known biological features of the cells (minimum trajectory length, valid position within the blood vessel, and volume range), to select the valid set of trajectories from the entire collection. ACME also incorporates a behavior detection module that performed non-supervised "behavior" discovery, hierarchically arranges the behavioral space and selects the most prominent features for each subset of behaviors.

Other image analysis platforms, such as Imaris, can be used however they should be adapted to the challenging conditions of the cremasteric vessels. A detailed technical description of ACME and its features will be described in future studies.

For the screening analyses in the cremaster muscle we used 2D imaging (epifluorescence) and static (one time point only) 3D spinning disk imaging. For these analyses we favored parameters that discriminated B3-type behavior (see Extended Data Fig.7A), that could be extracted by 2D imaging, and among morphometric features those that used relative (rather than absolute) measures within the same cell, such as H/L ratios and cell shape. 2D motility analysis of crawling neutrophils in vessels, we used Fiji/ImageJ with the help of the Manual Tracking plugin (Fabrice Cordeliperes, Institut Curie, France). The plug-in allowed tracking neutrophil displacement by calculating X and Y positions relative to the direction of blood flow and automatically computed total displacement, directionality and instantaneous velocities of cells. To analyze the morphology of neutrophils in our 3D confocal reconstructions, we used the 'Cell' function of Imaris.

Data analysis

We implemented parameter selection combined with dimensional reduction methods to enhance cell classification of our behavioral analyses (see Extended Data Fig.1). However, use of standard pipelines used for single cell RNA sequencing (such as Seurat4) can be also implemented for these analyses without the need of supervised parameter selection which should be validated using "training" experiments similar to the ones used shown in Figure 1 of this manuscript. Various pipelines for data analyses were used for the different experimental datasets, as summarized in Table S4. We did not perform data normalization in any of our imaging analyses since the absolute values for any given parameter were comparable between cells of each experiment.

Trachea dataset. For the analysis of the trachea datasets, we uploaded the final *raw* file to R Studio, including all the parameter values for each cell and time point, as well as their cell type defined by fluorescence protein expression (GFP and YFP). From the total set of 118 acquired and measured parameters we selected 31 that avoided redundancy or parameters with arbitrary values (e.g., positional parameters), and their distribution and correlation visualized in the corresponding correlation network (see Extended Data Fig.1 and Data S1). We also stored information of the identity of each cell based on its fluorescence profile that was only used to calculate the LRI/ARI values for each parameter. The input expression matrix, consisting of the 31 parameters and 7008 cell reconstructions (corresponding to 343 individual cells), was scaled with the R base *scale* function, was used to perform non-linear reduction to generate tSNE plots (function *Rtsne* from the package Rtsne). The resulting coordinates of tSNE were represented using the *ggplot2* package of RStudio. We then generated unbiased classification of cells over the tSNE representation using information from the fluorescence reporter mice (which were not used for data analysis), and projected the cell type over these clusters to assess accuracy of the behavioral analyses. We then analyzed each cell type from the individual clusters by excluding the non-dominant cell-type in each group (DCs in cluster 1, neutrophils in cluster 2) and subsetted them from the original representation using the *Rtsne* function, using the ggplot2 package for visual representation of each subset, and plotting the parameter value distribution for each group. To identify the differentially scored parameters between the two clusters, we

selected those that showed at least 0.25-fold difference (log-scale) between the two groups and used Seurat v4 [38] for selection and plot generation.

Ischemia reperfusion and laser injury dataset. For the analysis of both ischemia-reperfusion injury (I/R) and laser injury (LI) data, we uploaded the final raw files to R Studio, which included all the measured parameter values belonging to each cell at each time point (object), as well as the actual identity of each cell (neutrophil, DC or macrophage), which was known beforehand and was used only for validation analyses. We used the same set of selected parameters (see Extended Data Fig.1 and Data S1) to generate an input parameter expression matrix containing 31 parameters for 49436 cell time points (objects: corresponding to 4635 unique cells) in the I/R dataset, and for 32323 cell time points (objects) corresponding to 1228 individual cells in the laser injury dataset. We transformed the original matrix to a Seurat object and scaled the parameters. We performed Principal Component Analysis (PCA) to reduce the dimensionality to the four top principal components in both cases. Cells were clustered based on k-nearest neighbor graph using the Louvain algorithm. Finally, a non-linear reduction technique (tSNE) was performed to visualize the data in a low-dimensional space. We used the ggplot2 package for the visual representation of each subset and for plotting the parameter value distribution for each group. The Seurat object was finally subsetted according to the different cell types within the object to generate the corresponding tSNE plots. Each cluster corresponding to each cell type was plotted separately and the expression of every parameter over these clusters was projected again with ggplot2. The Seurat object was subsetted for the clusters obtained (Clusters 0 to 2) to identify sub-clusters within each cluster. Finally, we used Seurat to estimate the differentially scored parameters and to generate the heatmaps these parameters

Cremaster data. Raw data was uploaded to RStudio. The input parameter expression matrix had 73 parameters for 7098 cell points (objects), corresponding to 459 unique cells, including metadata information. We first transformed the data matrix to a Seurat Object and the parameters were scaled. Using Seurat we performed Principal Component Analysis (PCA) to reduce the dimensionality to the four top principal components and generated UMAP plots of the dataset. We used the UMAP reduction method to better capture the relationship between the different behavioral states of intravascular neutrophils in the cremaster experiments, since inter-cluster relationships are better captured by this dimensional reduction method. Based on the groups of cells visually identifiable in the UMAP plots we then performed supervised clustering using as reference the coordinates of the three visually defined groups. We performed manual gating over the UMAP representation and assigned to each cluster an unbiased classification (group/behavior 1, 2 and 3), adding a new metadata label that was used henceforth. To obtain the density plots over the UMAP representation, we used stat_density_2d_filled from the ggplot2 package. Using this segregated dataset, we generated a global heatmap with all parameters to group the cells hierarchically (with either three or five behaviors), and generated violin plots to compare the score of selected parameters based on the selected behavior. Finally, to identify the differentially scored parameters between groups we used a univariate model to determine outstanding predictors, divided according to their time dependency: for time-independent parameters we used a multinomial model with multinom function (nnet package) [39], and for time-dependent parameters we used logistic regression with glmer function (package lme4) [40], comparing all behaviors between them. The p-value threshold was set to 0.01.

Non-supervised clustering and behavioral transitions in the cremaster analyses

To analyze transitions of cells within behavioral groups of the cremaster dataset, we first performed non-supervised clustering discovery using the behavior detection module from ACME. This module selected the optimal number of behaviors (K) and organized cell objects into K clusters using a high-dimensional K-means algorithm [41]. In brief, K was selected by minimizing histogram intersection between behavior proportions in the two main differential groups (control vs. platelet-depletion), resulting in a K of 5. To represent this clusterization in two dimensions we used UMAP supervised by the 5 behaviors that were obtained from the K-means algorithm. The UMAP algorithm minimized the divergence of topological representations between the N-dimensional (73D) and the n-dimensional spaces (2D). The supervision of this algorithm built a new representation that combined the original representation (unsupervised) with a new representation (supervised) in which samples that do not belong to the same behavior are farther apart depending on the regularizing parameter α. Finally, to calculate the transitions between groups, we examined the trajectories of each neutrophil over time to identify transitions from one behavior to another. We set a minimum threshold of permanence (*pth*) equal to 3, so that a neutrophil must remain at least *pth* instants (3 time points) in the destination behavior for it to be considered a transition.

Mathematical modeling

We used logistic regression to analyze the complete set of 118 (kinetic and morphometric) variables measured in cells extracted from the trachea imaging dataset. Since previous information on leukocyte identities (DCs and neutrophils) was available, we computed for each variable the likelihood ratio index (LRI). To calculate the LRI, we used the McFadden LRI (R_{MCF}^2), which varies from 0 to 1 and provides a normalized measure of the classification capability of a logistic regression-based model with respect to a purely random model. R_{McF}^2, defined as $R_{MCF}^2 = 1 - [\log(L_M)/\log/(L_0)]$, where L_M and L_0 are the likelihoods for the model being fitted and the null model, respectively. If the model being fitted had no predictive ability, its likelihood value would only be slightly greater than the likelihood of the null (i.e. purely random) model, and thus LRI would be close to zero, whereas models explaining most of the variability in the observations yields a LRI close to one.

This method was combined with a correlation analysis that allowed us to construct a correlation network providing the hierarchy of variables displaying the most accurate classification prediction to identify both types of leukocytes. This network was built using multidimensional scaling techniques, employing Pearson's distances as entries of the dissimilarity matrix. We subsequently calculated the LRIs of multivariable combinations from random samples of the complete set (118 variables), as well as reduced sets consisting of 50, 25 and 10 variables. From these, we produced series of violin plots using kernel density estimations with standard Gaussian kernel functions, and utilized the observed trends to build a qualitative stochastic model capturing the relationship between the fraction of all known behavioral variables vs. a normalized classification index (with 1 representing perfect identification of cell type, and 0 random assignment). In this stochastic model, the classification was dichotomous whereas each of the independent synthetic parameters (a total of 100) were generated from a half-normal distribution with equal scale parameter, with their outcomes being nonnegative real

numbers (1000 replicas per parameter). The relationship between the dependent parameter and the independent ones was modelled via a logistic function. We then created combinations of random samples with a fixed number (ranging from 1 up to 100) of synthetic variables and computed the corresponding LRIs. These LRIs gave rise to a learning (banded) curve that depended on the percentage of variables used.

For analysis of the cremaster dataset we extended the previous approach to the set of 73 variables extracted. We employed a statistical model based on decision tree learning (a classification and regression tree algorithm). Information on leukocyte states based on imaging analyses based on non-supervised clustering was used to classify the cells in behaviors 1-3. To quantify the accuracy of the classification, we employed the Adjusted Rand Index (ARI). Combining this metric with the construction of a new correlation network, by means of multidimensional scaling techniques, we obtained a new hierarchy of variables. We used RStudio for the analyses of the two datasets. Violin plots were created employing the vioplot R package, while correlation networks were built using the igraph R package.

Generation of bone marrow transplanted mice and mixed bone marrow chimeras
In order to homogenize hosts for all mutant mice and to provide internal controls, we generated both full donor or mixed bone marrow chimeric mice by bone marrow transplantation. For full marrow chimeras, we harvested bone marrow cells from C57BL/6 or mutant donors by flushing the femur with PBS. We then injected 1 million bone marrow nucleated cells by intravenous injection to recipient wild-type C57BL/6 mice or CD45.1 congenic mice after lethal irradiation (two 6Gy doses, 3 h apart).
For the mixed bone marrow chimeras, we harvested donor bone marrow cells from DsRed^{Tg} and non-fluorescent experimental mutant models (see Table S1) and injected 1 million of a bone marrow nucleated cell mixture from both donors by intravenous injection into lethally irradiated C57BL/6 recipients, as indicated above. 6–8 weeks after transplantation, we assessed engraftment and chimerism of recipient animals in blood by flow cytometry before further experimentation.

Myocardial ischemia-reperfusion (infarction)
To estimate effects of genes or treatments on infarct size, we subjected 8- to 15-week-old male mice to 45 min occlusion of the left anterior descending (LAD) coronary artery followed by 1h reperfusion. We performed I/R procedure as previously reported [11]. Briefly, fully anesthetized animals were intubated, and temperature controlled throughout the experiment at 37.5°C to prevent hypothermia-driven cardioprotection. Then, we performed thoracotomy and ligation of LAD with a nylon 8/0 monofilament suture for 45 min, and monitored the electrocardiogram (MP36R, Biopac Systems Inc.) to confirm total coronary artery occlusion (ST-segment elevation) throughout the 45 min ischemia. At the end of the ischemia, we closed the chest and animals were kept with 100% O_2 and treated with buprenorphine (subcutaneous injection, 0.1 mg/kg). For quantification of infarct size, we re-anesthetized and re-intubated the mice, and re-occluded the LAD coronary by ligating the suture in the same position as the original infarction. Then, animals were sacrificed and 1 ml of 1% Evans Blue dye (Sigma) was infused IV to delineate the Area at Risk (AAR: myocardium lacking blood flow, i.e., negative for blue dye staining). The left ventricle (LV) was isolated, cut into transverse slices (5-7 1-mm thick slices per LV), and both sides were imaged. To delineate the infarcted (necrotic) myocardium, we incubated slices in triphenyltetrazolium chloride (TTC, Sigma) at 37°C

for 10 min. Next, we took new images and weighed the slices. Finally, we quantified regions negative for Evans Blue staining (AAR) and for TTC (infarcted myocardium) using ImageJ (NIH, Bethesda, MD). Percentage values for AAR and infarcted myocardium were corrected for weight (mg) independently for each slice. Absolute AAR and infarct size were determined as the mg:mg ratio of AAR:LV and infarcted myocardium:AAR, respectively. We assessed each sample blind to condition (mouse type or treatment).

For permanent myocardial Infarction, we subjected male 8 to 12-week-old mice to permanent occlusion of the left anterior descending (LAD) coronary artery for cardiac function and fibrosis measure. We measured cardiac function at basal time and days 3 and 28 post occlusion by echocardiography using a Vevo 2100 Ultra High Frequency ultrasound with support of the Advanced Imaging Unit of CNIC, and stained heart slices with hematoxylin / eosin to measure fibrosis.

Nephrotoxic injury and vascular permeability assay
To induce nephrotoxic injury we first pre-conditioned female mice (8–12 weeks of age) by intraperitoneal injection of 0.1ug/g of Lipopolysaccharide from *Escherichia coli* 0111:B4 (LPS; Sigma) alone (LPS only) or together with intravenous injection of 5 µl/g of sheep anti-mouse glomerular basement membrane nephrotoxic serum (batch number 90252, as in [42]) diluted with sterile PBS. Urine and plasma were obtained at day 2 post kidney injury induction for biochemical analysis performed with a Dimension RxL Max Integrated Chemistry System (Siemens Healthineers). For vascular permeability assays in the kidney, we intravenously injected 200 µl of 0.5% solution of Evans blue in sterile PBS into mice induced for nephrotoxic injury. After 15 min, we sacrificed mice and extracted kidneys for weight and leakage. To measure leakage, we submerged kidneys in tubes containing 0.5 ml formamide at 55 °C for 24 h. After incubation, we centrifuged the tubes for 5 min at 645g and collected the supernatant. Finally, we measured the absorbance of supernatants at 610 nm using an xMark Microplate Spectrophotometer (BioRad) plate reader.

Infection models
Mice were intravenously infected with 1.25 x10^5 colony-forming units (CFUs) of *C. albicans* (SC5314 strain) or with 2.5x10^7 CFUs of *S. aureus* (RNU4220 strain) and monitored for weight loss and general health following our institutional guidance. In the *C. albicans* infection model, we determined kidney weight and fungal burden at day 6 post-infection by plating organ homogenates in serial dilutions on YPD plates (Sigma). CFUs were counted after growth for 48 hours at 30°C. During staphylococcal infection, blood was collected at various time points for hematology.

In vivo NET formation during ischemia/reperfusion
To perform ischemia/reperfusion in the cremaster muscle, we exteriorized the tissue as described[10] and induced ischemia by clamping the tissue connecting the muscle to the body with a 15-mm Micro Serrefine clamp (Fine Science Tools) for 45 min. Subsequently, we accomplished reperfusion by removal of the clamp. 15 min after reperfusion we euthanized mice and the muscle was removed for analysis. We fixed the excised muscles in 4% paraformaldehyde (PFA) at 4 °C overnight and then we washed them three times in PBS containing 0.5% Triton X-100 (PBST) and blocked for 2 h in PBST

25% fetal bovine serum (FBS) at room temperature with shaking. We stained the samples with anti-cit-H3, anti-MPO and anti-CD31 in 10% FBS-PBST overnight at 4 °C with shaking. We then added secondary antibodies in 10% FBS-PBST for 4 h at room temperature. After secondary staining, we washed and mounted the samples in Mowiol 4-88 (31KDa; Sigma). We performed imaging of whole-mount cremaster muscles using a Nikon A1R confocal system coupled to a Nikon Eclipse-Ti inverted microscope with the following lines: diode 402 nm, argon laser 457, 476, 488, 514 nm, diode 561 nm, HeNe laser 642 nm using a Plan Apo 10×/0.45 dry objective and the software NIS Elements AR v.4.30.02 (Build 1053 LO, 64 bits, Nikon Instruments). We analyzed the images using Imaris (Bitplane). All imaging was performed at the Microscopy and Dynamic Imaging Unit of CNIC.

Transmission Electron Microscopy (TEM)
For TEM analysis of mouse tissues, we fixed heart and kidney pieces in 1% glutaraldehyde and 4% PFA in PBS, overnight at 4°C. Samples were post fixed in 1% osmium tetroxide for 60 minutes and dehydrated through a series of ethanol solutions (30%, 50%, 70%, 95%, and 100%) and acetone. After the last dehydration step, we incubated the samples in a 1:3, 1:1, 3:1 mixture of Durcupan resin and acetone and cured at 60° for 48h. We obtained ultrathin sections (50-60 nm) using a diamond knife (Diatome) in an ultramicrotome (Leica Reichert ultracut S) and collected them in 200-mesh copper grids. We then counterstained the sections with 2% uranyl acetate in water from 20 min followed by a lead citrate solution. After staining, we examined the samples with a JEOL JEM1010 electron microscope (Tokyo, Japan) equipped with an Orius SC200 digital camera (Gatan Inc.) at the Transmission Electron Microscopy Laboratory (Interdepartmental Research Service, UAM). We analyzed heart images with ImageJ by counting the total number of vacuoles and Weibel-Palade bodies per μm^2 present on the endothelial cells of the blood vessel wall.

Neutrophil in vivo recruitment assays
Mixed chimeric mice generated by bone marrow transplantation of wild-type together with the indicated mutant mice were used for these experiments. For the model of Zymosan-Induced Peritonitis, we treated the transplanted chimeras with zymosan (1mg, intraperitoneal injection, Sigma). After 2 h, we took blood samples and performed peritoneal lavage for cytometric analyses and cell counts. We compared the ratios of neutrophils in the peritoneum vs. blood from each donor to estimate the recruitment efficiencies of mutant cells (ratio in peritoneum / ratio in blood).
For the LPS-induced lung injury, anesthetized mice were allowed to inhale 10 µl of 5mg/ml of Lipopolysaccharides from Escherichia coli 0111:B4 (LPS) (Sigma) solution. The solution was placed drop by drop, while holding the mouse tongue, over the mouse nostrils and let the whole droplet to be inhaled before placing more solution to avoid suffocation. After 24h, we performed Bronchoalveolar Lavage (BAL) in the LPS-treated mice. We euthanized the mice by injecting 100 µl of Pentobarbital Sodium (Dolethal) 200 mg/ml intravenously. Then we performed an incision over the mouse throat and pulled the salivary glands over to the sides to expose the trachea muscles. We dissected the trachea muscles with tweezers and exposed the airway. Using a 18G needle coupled to 1ml syringe with 1ml PBS, we pierced through soft trachea tissue and slowly injected the PBS. After 10-15 seconds, we recovered the lavage. We analyzed the absolute numbers of neutrophils by flow cytometry after staining with an anti-Ly6G antibody.

Statistical analysis

Unless otherwise indicated, data are represented as mean ± standard error of the mean, and analyzed using Prism software (GraphPad, Inc.). Datasets were analyzed by a D'Agostino-Pearsons normality test to define normality and implement the appropriate statistical test. Data consisting of only two data sets were analyzed using two-tailed Student´s t-test unless otherwise stated. To identify statistically significant differences for treatment/genotype over time or more than two datasets we used two-way ANOVA or one-way ANOVA with Tukey's or multiple comparisons tests, respectively. A p-value below 0.05 was considered statistically significant. P-values are represented as follows: $p < 0.05$ (∗), $p \leq 0.01$ (∗∗) and $P \leq 0.001$ (∗∗∗), and nonsignificant differences (n.s.) are indicated.

Captions for Movies S1 to S5

Movie S1 caption. Multiphoton imaging of leukocytes in influenza-infected trachea. Representative 3D image sequence of inflamed trachea from a CD11c^{YFP} mouse at 3 days post-infection with PR8 influenza virus. The left panel shows raw imaging data capturing the shape and movement of DCs (red) and adoptively transferred CK6^{ECFP} neutrophils (green) within the tracheal collagen fibers (SHG, blue). The movie at right shows the corresponding 3D surface reconstructions of the cells (also referred to as 'objects', grey) and their tracks (red), which combined were used for the morpho-kinetic analysis in Figure 1B. Tracks only show the trajectories of the cells during the last 7 time points to avoid crowding. Scale bar, 50µm. Total elapsed time: 30 min. The movie is played twice.

Movie S2 caption. Multiphoton imaging of leukocytes during ischemia-reperfusion injury. Dynamic imaging of the ear skin of LyzM^{GFP}; CD11c^{YFP} mice subjected to I/R. 4D intravital images were acquired after pressing magnets were removed (4h post reperfusion). The top panel corresponds to raw images where DCs are visualized in red, neutrophils in green and macrophages in light green. SHG shown in blue corresponds to the collagen matrix. The I/R area is at the left side of the image where neutrophil density exponentially increases after reperfusion. The bottom panel shows the corresponding 3D surface reconstruction of cells ('objects', grey) and their tracks (red), which were used for the morpho-kinetic analysis represented in Figure 1H. Tracks represent the trajectories of cells during the last 7 time points. Scale bar, 20µm. Total elapsed time: 2 h 55 min. The movie is played twice.

Movie S3 caption. Multiphoton imaging of DCs and neutrophils during laser-burn injury. 3D image sequences of the ear skin of LyzM^{GFP}; CD11c^{YFP} mice after laser-induced focal sterile injury. The movie at left displays raw imaging data with DCs in red and neutrophils in green. SHG is shown in blue (collagen) and blood vessels and the burnt area are in grey (Evans blue and autofluorescence). The right panel shows the corresponding 3D surface reconstruction of cells ('objects', grey) and their tracks (red), which were used for the morpho-kinetic analysis in Figure 1I. Tracks represent the trajectories of cells during last 7 time points. Scale bar, 50µm. Total elapsed time: 2h 30 min. The movie is played twice.

Movie S4 caption. Spinning-disk imaging of inflamed venules for behavioral analysis of intravascular neutrophils. Representative 3D image sequence of an inflamed cremaster venule from a LyzM^{GFP} mouse showing leukocytes rolling and adhering (grey) to the vessel wall (blue, CD31). The tracks of crawling neutrophils are depicted in red for a maximum period of 7 time points. The morpho-kinetic information for intravascular neutrophils was extracted from a set of similar recordings and were used for the analyses shown in Figure 2D. Scale bar, 20µm. Total elapsed time: 6 min. The movie is played twice.

Movie S5 caption. Three behavioral states for intravascular neutrophils within inflamed venules. 4D image sequences of representative intravascular neutrophils (red) from behavioral groups 1-3 defined in Figure 2E. Behavior 1 is associated with small, egg-shaped neutrophils sessile on the vascular wall (blue, CD31). Behavior 2 neutrophils are characterized by ameboid-shape and faster motion, with frequent changes in shape. Behavior 3 neutrophils are large and sessile, and in intimate contact with the vascular wall. Scale bar, 5µm. Total elapsed time: 6 min. The movie is played twice.